Constraining the top-Higgs sector of the standard model effective field theory

V. Cirigliano, W. Dekens, J. de Vries, and E. Mereghetti

Phys. Rev. D **94**, 034031 — Published 19 August 2016

DOI: 10.1103/PhysRevD.94.034031

LA-UR-16-23433
NIKHEF 2016-017

Constraining the top-Higgs sector of the Standard Model Effective Field Theory

V. Cirigliano[a], W. Dekens[a,b], J. de Vries[c], and E. Mereghetti[a]

[a] *Theoretical Division, Los Alamos National Laboratory, Los Alamos, NM 87545, USA*

[b] *New Mexico Consortium, Los Alamos Research Park, Los Alamos, NM 87544, USA*

[c] *Nikhef, Theory Group, Science Park 105, 1098 XG, Amsterdam, The Netherlands*

Abstract

Working in the framework of the Standard Model Effective Field Theory, we study chirality-flipping couplings of the top quark to Higgs and gauge bosons. We discuss in detail the renormalization group evolution to lower energies and investigate direct and indirect contributions to high- and low-energy CP-conserving and CP-violating observables. Our analysis includes constraints from collider observables, precision electroweak tests, flavor physics, and electric dipole moments. We find that indirect probes are competitive or dominant for both CP-even and CP-odd observables, even after accounting for uncertainties associated with hadronic and nuclear matrix elements, illustrating the importance of including operator mixing in constraining the Standard Model Effective Field Theory. We also study scenarios where multiple anomalous top couplings are generated at the high scale, showing that while the bounds on individual couplings relax, strong correlations among couplings survive. Finally, we find that enforcing minimal flavor violation does not significantly affect the bounds on the top couplings.

1 Introduction

More than twenty years after its discovery at the Tevatron [1, 2], the top quark is nowadays copiously produced at the Large Hadron Collider (LHC) and is at the forefront of searches for physics beyond the Standard Model. In fact, in several scenarios, including partial compositeness [3], warped extra dimensions [4], supersymmetric models with light stops relevant for electroweak baryogenesis [5], enhanced deviations from the SM are expected in the top sector. The top quark is the fermion with the strongest coupling to the Higgs. The dominant Higgs production mechanism in the SM, the Higgs width, and several important decay channels, are therefore sensitive probes of top-Higgs couplings. At the same time, the anomalous top-Higgs couplings affect via quantum corrections processes that do not necessarily involve a top quark and/or a Higgs boson. Such "indirect probes" give valuable complementary information and, as we demonstrate here, can constrain non-standard top-Higgs couplings more strongly than direct searches.

In this article we discuss direct and indirect probes of chirality-flipping top couplings to gauge bosons and the Higgs, including both CP-conserving (CPC) and CP-violating (CPV) interactions. This set of interactions gives rise to an interesting list of phenomena ranging from signals in low-energy precision tests to deviations from SM predictions in proton-proton collisions at the LHC. Additional interactions that do not change the chirality of the top quark also appear at the dimension-six level. We will not consider these terms in this work. A lot has been written already about top-gluon [6–17], top-photon [18–22], top-W [23–33], top Yukawa [34–43] couplings, and global analyses [44–49]. Throughout this work we often use results and insights from these papers. The main features of our work are:

- We perform a systematic analysis of the renormalization-group equations of the top-Higgs operators including QCD and electroweak corrections. This is crucial in obtaining the strongest constraints on the set of top-Higgs couplings as in many instances indirect observables are more sensitive than direct observables.

- We investigate in detail the impact of measurements of electric dipole moments (EDMs) [18, 35, 44, 50, 51]. A major finding of our analysis is that even after taking into account the hadronic and nuclear uncertainties [51], EDMs dominate the bounds on all the CPV top couplings. In particular, as we reported in Ref. [52], bounds on the top EDM (weak EDM) are improved by three orders of magnitude over the previous literature. The new constraints on the CPV top couplings lie well below prospected sensitivities of collider searches.

- We present a comprehensive analysis of direct and indirect constraints, the latter arising from both high- and low-energy, including up-to-date indirect constraints from Higgs production and decay at the LHC. We show that constraints from Higgs production and decay signal strengths are competitive with respect to observables involving top final states.

- We derive bounds on anomalous couplings under three assumptions: first, we only allow one operator at a time to be generated at the high scale (including both CPC and CPV couplings). Second, we perform a global analysis where all chirality-flipping top-Higgs couplings are generated at the high scale and we investigate how the constraints on the individual couplings are softened due to cancellations between different operators. Finally,

we apply the framework of Minimal Flavor Violation in which the top-Higgs couplings are related to couplings involving lighter quarks.

We work in the framework of the linear SM Effective Field Theory (SM-EFT) [53–57]. We assume that there is a gap between the scale of new physics Λ and the electroweak scale $v = 246$ GeV and keep only the leading terms in $(v/\Lambda)^2$, corresponding to dimension-six operators. We assume that at the high-scale Λ the largest non-standard effects appear in the top sector, and hence set to zero all other couplings. We then evolve the non-standard top couplings to lower scales through renormalization group flow and heavy SM particle thresholds. The evolution induces operators that impact a number of high-energy and low-energy phenomena, thus leading to constraints on non-standard top-Higgs couplings at the scale Λ.

Direct probes involve top quark production (single top, $t\bar{t}$, and $t\bar{t}h$) and decay (W boson helicity fractions, lepton angular distributions) at colliders. We include CPV effects in the angular distributions of the decay products of a single top [58], while we neglect CPV observables in $t\bar{t}$ and $t\bar{t}h$ production/decay [43, 59–67] as these are not yet competitive. However, as the number of independent low-energy CPV observables is limited, future measurements of CPV observables at colliders can play an important complementary role. Indirect probes involve top quarks in quantum loops, affecting both high-energy (Higgs production and decay, precision electroweak tests) and low-energy observables ($b \to s\gamma$ and EDMs).

The paper is organized as follows. In Section 2 we set up the operator analysis by discussing the high-scale top operators and identifying the relevant operators that are induced by operator mixing. In Section 3 we present the renormalization group equations (RGEs) needed to evolve the anomalous top couplings from high-scale to the energy scales associated to a variety of observables (ranging from collider to atomic EDMs). We discuss direct and indirect constraints from collider observables in Section 4, and the impact of precision electroweak measurements in Section 5. Indirect bounds from flavor physics and EDMs are discussed in Sections 6 and 7, respectively. We then present our fitting strategy (Section 8) and results (Section 9). We cast our analysis into the framework of Minimal Flavor Violation (Section 10) before presenting our conclusions (Section 11).

2 Operator structure

In this work we study chirality-flipping interactions involving the top quark and the Higgs boson. At dimension six, five such interactions appear in the complete set of gauge-invariant operators [53, 54]. In their $SU(3)_c \times SU(2) \times U(1)_Y$ invariant forms these operators consist of a hypercharge dipole, gluonic dipole, a non-standard Yukawa coupling, and two electroweak dipoles,

$$\begin{aligned}\mathcal{L}_{\text{eff}}^{\text{BSM}} \;=\; & -\frac{g'}{\sqrt{2}}\,\bar{q}_L\sigma^{\mu\nu}B_{\mu\nu}\,\Gamma_B^u\,u_R\,\tilde{\varphi} - \frac{g_s}{\sqrt{2}}\,\bar{q}_L\sigma^{\mu\nu}G^a_{\mu\nu}t^a\,\Gamma_g^u\,u_R\,\tilde{\varphi} - \sqrt{2}\varphi^\dagger\varphi\;\bar{q}_L\,Y_u'\,u_R\,\tilde{\varphi} \\ & -\frac{g}{\sqrt{2}}\,\bar{q}_L\sigma^{\mu\nu}W^a_{\mu\nu}\tau^a\,\Gamma_W^u\,u_R\,\tilde{\varphi} - \frac{g}{\sqrt{2}}\,\bar{q}_L\sigma^{\mu\nu}W^a_{\mu\nu}\tau^a\,\Gamma_W^d\,d_R\,\varphi + \text{h.c.}. \end{aligned} \tag{1}$$

Here q_L represents the left-handed quark doublet, u_R and d_R are the right-handed quark singlets, and φ is the Higgs doublet ($\tilde{\varphi} = i\tau^2\varphi^*$). $B_{\mu\nu}$, $W^a_{\mu\nu}$, and $G^a_{\mu\nu}$ are the fields strengths of the $U(1)_Y$, $SU(2)$, and $SU(3)_c$ gauge groups, while g', g, and g_s denote their gauge couplings and $\tau^a/2$ and t^a are the $SU(2)$ and $SU(3)_c$ generators, respectively. Our conventions are such that the covariant

derivative is given by $D_\mu = \partial_\mu - ig_s t^a G^a_\mu - i\frac{g}{2}\tau^a W^a_\mu - ig' Y B_\mu$, with Y the hypercharge. The couplings Y'_u and $\Gamma^{u,d}_{g,B,W}$ have mass dimension -2 and generally form 3×3 matrices in flavor space.

At the same order in the SM-EFT expansion there appear additional anomalous interactions between top quarks and Higgs fields that do not change the chirality. Examples of such operators are $\varphi^\dagger \vec{\tau} \overleftrightarrow{D}_\mu \varphi\, \bar{q}_L \vec{\tau} \gamma^\mu q_L$ and $\tilde{\varphi}^\dagger D_\mu \varphi\, \bar{u}_R \gamma^\mu d_R$. Such operators, to good approximation, do not mix under renormalization group flow with the chirality-changing operators and the operators in the extended basis introduced in Section 2.2, which therefore form a closed set. The chirality-conserving operators, however, could impact the global constraints that can be set on the operators studied in this work. We comment on this in Section 9.2.

Working in the unitary gauge, in which the Higgs doublet takes the form $\varphi = (0,\, v+h)^T/\sqrt{2}$, one sees that to $\mathcal{O}(h^0)$ the couplings Y'_u then contribute to the up-type quark mass matrix. After absorbing these contributions into the SM quark mass matrix, and moving to the physical (mass) basis, the resulting effective Lagrangian encoding non-standard top couplings (neglecting flavor-changing neutral currents) at the high scale $\Lambda \gg v$ is [1]

$$\mathcal{L}_{\rm top} = \sum_{\alpha\in\{Y,g,\gamma,Wt,Wb\}} C_\alpha\, O_\alpha + \text{h.c.} \tag{2}$$

with complex couplings $C_\alpha = c_\alpha + i\,\tilde{c}_\alpha$ and

$$O_\gamma = -\frac{eQ_t}{2} m_t\, \bar{t}_L \sigma_{\mu\nu} \left(F^{\mu\nu} - t_W Z^{\mu\nu}\right) t_R \left(1+\frac{h}{v}\right) \tag{3a}$$

$$O_g = -\frac{g_s}{2} m_t\, \bar{t}_L \sigma_{\mu\nu} G^{\mu\nu} t_R \left(1+\frac{h}{v}\right) \tag{3b}$$

$$O_{Wt} = -g m_t \left[\frac{1}{\sqrt{2}} \bar{b}'_L \sigma^{\mu\nu} t_R W^-_{\mu\nu} + \bar{t}_L \sigma^{\mu\nu} t_R \left(\frac{1}{2c_W} Z_{\mu\nu} + i g W^-_\mu W^+_\nu\right)\right]\left(1+\frac{h}{v}\right) \tag{3c}$$

$$O_{Wb} = -g m_b \left[\frac{1}{\sqrt{2}} \bar{t}'_L \sigma^{\mu\nu} b_R W^+_{\mu\nu} - \bar{b}_L \sigma^{\mu\nu} b_R \left(\frac{1}{2c_W} Z_{\mu\nu} + i g W^-_\mu W^+_\nu\right)\right]\left(1+\frac{h}{v}\right) \tag{3d}$$

$$O_Y = -m_t \bar{t}_L t_R \left(vh + \frac{3}{2}h^2 + \frac{1}{2}\frac{h^3}{v}\right)\,, \tag{3e}$$

where $Q_t = 2/3$, $t_W = \tan\theta_W$, $c_W = \cos\theta_W$, with θ_W the Weinberg angle. The physical photon and Z boson fields are given by $Z_\mu = c_W W^3_\mu - s_W B_\mu$ and $A_\mu = c_W B_\mu + s_W W^3_\mu$. Finally, the operators $O_{Wt,Wb}$ contain the combinations $b' = V_{tb} b + V_{ts} s + V_{td} d$, and $t' = V^*_{tb} t + V^*_{cb} c + V^*_{ub} u$. The relation between these operators in the quark mass basis and their $SU(2)\times U(1)_Y$ invariant forms is given in Table 1.

The couplings C_α have mass dimension $[-2]$ and are related to properties of the top quark, such as the electric and magnetic dipole moments ($d_t = (e m_t Q_t)\tilde{c}_\gamma$ and $\mu_t = (e m_t Q_t) c_\gamma$), their non-abelian gluonic counterparts ($\tilde{d}_t = m_t \tilde{c}_g$ and $\tilde{\mu}_t = m_t c_g$), and the Higgs-top, W-top, and Z-top couplings.

We assume that at the high-scale Λ the largest non-standard effects appear in the top sector, and hence set to zero all other couplings. We then evolve the non-standard top couplings to

[1] Denoting the Standard Model Yukawa couplings by $\mathcal{L}_Y \supset -\sqrt{2}\bar{q}_L Y_u u_R \tilde{\varphi}$, the up-type quark mass matrix is $m_u = v\left(Y_u - \frac{v^2}{2} Y'_u\right)$. Upon expressing $\mathcal{L}_Y + \mathcal{L}^{\rm BSM}_{\rm eff}$ in terms of m_u and Y'_u, we get $\mathcal{L}_Y + \mathcal{L}^{\rm BSM}_{\rm eff} \supset -\frac{m_t}{v}\bar{t}th + (C_Y O_Y + \text{h.c.})$, with the relation between C_Y and $[Y'_u]_{33}$ given in Table 1.

lower scales through renormalization group flow and heavy SM particle thresholds. The evolution induces operators that impact a number of high-energy and low-energy phenomena (of which many do not involve the top quark directly), thus leading to constraints on non-standard top-Higgs couplings at the scale Λ.

2.1 Mixing Structure

A consistent field-theoretical analysis of the phenomenological implications of the effective Lagrangian (2) requires extending the operator basis to include all the operators which O_α ($\alpha \in \{Y, g, \gamma, Wt, Wb\}$) can mix into. We will consider the leading-logarithm contributions and include the effects induced by the Standard Model gauge couplings g_s, g, g', and the top Yukawa coupling y_t.

Let us first consider the dipole operators $O_{\gamma,g,Wt,Wb}$, that belong to the $\psi^2 HX$ category in the notation of Refs. [54–57]:

- At one loop, $O_{\gamma,g,Wt,Wb}$ mix into gauge-Higgs operators (X^2H^2 in the notation of Refs. [54–57]) and into dipole operators $\psi^2 HX$ with different flavor structures. In the latter group, of particular phenomenological interest are the flavor diagonal light-flavor dipoles and the $b \to s$ dipoles. Note also that the gauge-Higgs operators (X^2H^2) mix back into the dipoles of any flavor.

- The top dipoles $O_{\gamma,g,Wt,Wb}$ mix into O_Y, with their respective gauge-coupling strengths. We retain only the mixing proportional to the strong coupling, i.e. that of O_g into O_Y.

- $O_{\gamma,g,Wt,Wb}$ also mix into four-fermion operators with chirality structure $(\bar{L}R)(\bar{L}R)$ [57], namely the four-quark operators $Q^{(1),(8)}_{quqd}$ and the semi-leptonic operator $Q^{(3)}_{lequ}$. These operators involve at least one third-generation quark (from the $O_{\gamma,g,Wt,Wb}$ vertex). While there are no strong phenomenological handles on these four-fermion operators [2], the semileptonic and four-quark operators $Q^{(3)}_{lequ}$ and $Q^{(1),(8)}_{quqd}$ mix back into the lepton and quark dipoles, respectively [3]. Thus, $Q^{(3)}_{lequ}$ and $Q^{(1),(8)}_{quqd}$ feed into the electron, mercury, and neutron EDMs, and we therefore include them in our extended basis.

- Finally, at the top quark threshold O_g and O_Y induce the Weinberg three-gluon operator $O_{\tilde{G}}$, which we therefore include in our extended basis.

The operator O_Y (ψ^3H^3 in the notation of Refs. [54–57]) mixes only into $O_H = (\varphi^\dagger\varphi)^3$, which we do not include in our phenomenological analysis as it does not contribute to any precision observable useful to put constraints on C_Y. On the other hand, O_Y contributes via threshold corrections to most of the operators mentioned above (X^2H^2, $O_{\tilde{G}}$, and the light fermion dipoles).

[2] The generated four-fermion operators involving only third-generations quarks and leptons are the least suppressed by CKM factors and Yukawa couplings, but they are the hardest to constrain as they do not contribute to very sensitive observables. On the other hand, operators involving light fermion generations might mediate $t\bar{t}$ or single-top production at colliders, but are induced at a much suppressed level, proportional to the light-fermion Yukawa couplings, thus leading to weak constraints on $C_{\gamma,g,Wt,Wb}$.

[3] The mixing of $Q^{(1),(8)}_{quqd}$ into the dipole operators had been noticed in Refs. [68, 69] and has been included in an updated version of Ref. [56]. We thank Aneesh Manohar for confirming our results.

2.2 Extended Operator Basis

Grouping the operators according to the processes they contribute to, we can write the effective Lagrangian at the high scale as

$$\mathcal{L}_{\text{eff}} = \mathcal{L}_{\text{SM}} + \mathcal{L}_{\text{top}} + \mathcal{L}_{\varphi\varphi XX} + \mathcal{L}_{\varphi\varphi X\tilde{X}} + \mathcal{L}_{(\bar{L}R)(\bar{L}R)} + \mathcal{L}_{b\to s} + \mathcal{L}_{\text{EDMs}} \tag{4}$$

where $\mathcal{L}_{\text{top}}$ is given in (2),

$$\begin{aligned}
\mathcal{L}_{\varphi\varphi XX} &= C_{\varphi G}O_{\varphi G} + C_{\varphi B}O_{\varphi B} + C_{\varphi W}O_{\varphi W} + C_{\varphi WB}O_{\varphi WB} && \text{(5a)}\\
\mathcal{L}_{\varphi\varphi X\tilde{X}} &= C_{\varphi\tilde{G}}O_{\varphi\tilde{G}} + C_{\varphi\tilde{B}}O_{\varphi\tilde{B}} + C_{\varphi\tilde{W}}O_{\varphi\tilde{W}} + C_{\varphi\tilde{W}B}O_{\varphi\tilde{W}B} && \text{(5b)}\\
\mathcal{L}_{b\to s} &= C_{\gamma}^{(bs)}O_{\gamma}^{(bs)} + C_{g}^{(bs)}O_{g}^{(bs)} + \text{h.c.} && \text{(5c)}\\
\mathcal{L}_{(\bar{L}R)(\bar{L}R)} &= C_{lequ}^{(3)}O_{lequ}^{(3)} + C_{quqd}^{(1)}O_{quqd}^{(1)} + C_{quqd}^{(8)}O_{quqd}^{(8)} + \text{h.c.} && \text{(5d)}\\
\mathcal{L}_{\text{EDMs}} &= \sum_{f=e,u,d,s,c,b}\left(C_{\gamma}^{(f)}O_{\gamma}^{(f)} + \text{h.c.}\right) + \sum_{q=u,d,s,c,b}\left(C_{g}^{(f)}O_{g}^{(f)} + \text{h.c.}\right) + C_{\tilde{G}}O_{\tilde{G}}\ , && \text{(5e)}
\end{aligned}$$

and the operators of the extended basis are explicitly given in Table 2. We will present the anomalous dimensions for the relevant mixing terms and the threshold corrections in Section 3. Eq. (4) will be the starting point of our phenomenological analysis, with all Wilson coefficients $C_\alpha(\Lambda)$ set to zero except for $\alpha \in \{Y, g, \gamma, Wt, Wb\}$.

Note that the operators in the extended basis contribute to a large number of CP-even and CP-odd observables both at high- and low-energies (see Tables 6 and 7 for a synopsis) that can thus be used to constrain the chirality-flipping top-Higgs couplings of Eq. (2). In particular:

- The Higgs-gauge operators in $\mathcal{L}_{\varphi\varphi XX}$ affect electroweak precision tests and Higgs production and decay processes. In particular, they contribute to $h \to \gamma\gamma$ ($C_{\varphi B,\,\varphi W,\,\varphi WB}$), $gg \leftrightarrow h$ ($C_{\varphi G}$), and the S parameter ($C_{\varphi WB}$), see Section 4 for details.

- The electromagnetic and strong dipole operators $O_{\gamma,g}^{(bs)}$ in $\mathcal{L}_{b\to s}$ contribute to $b \to s\gamma$ decays. The connection of $C_{\gamma,g}^{(bs)}$ to the BR$(b \to s\gamma)$ and $A_{CP}(b \to s\gamma)$ are discussed in Section 6.1.

- Finally the EDMs of light fermions, the chromo-EDMs (CEDMs) of light quarks, and the three-gluon Weinberg operator, contained in $\mathcal{L}_{\text{EDMs}}$, contribute to the EDMs of the electron, neutron, and diamagnetic atoms such as mercury. Although the operators involving the heavier quarks, c and b, do not contribute directly, they do facilitate indirect contributions to EDMs via threshold contributions to the coefficient $C_{\tilde{G}}$. The connection between the above interactions and EDMs is discussed in Section 7.

  It is important to note that the operators in $\mathcal{L}_{\text{EDMs}}$ can be induced via mixing in two ways. First, the top-Higgs couplings in $\mathcal{L}_{\text{top}}$ directly mix into the quark (color-)EDMs, through one-loop diagrams. Second, the CP-odd Higgs-gauge operators in $\mathcal{L}_{\varphi\varphi X\tilde{X}}$ and four-fermion operators in $\mathcal{L}_{(\bar{L}R)(\bar{L}R)}$ mix into the light-fermion EDMs and light-quark chromo-EDMs. In a leading logarithm analysis both effects have to be included, as the operators in $\mathcal{L}_{\text{top}}$ mix into $\mathcal{L}_{\varphi\varphi X\tilde{X}}$ [4] and $\mathcal{L}_{(\bar{L}R)(\bar{L}R)}$. This leads to a two step path $\mathcal{L}_{\text{top}} \to \mathcal{L}_{\varphi\varphi X\tilde{X},\,(\bar{L}R)(\bar{L}R)} \to \mathcal{L}_{\text{EDMs}}$ connecting the top-Higgs electroweak dipoles to the light fermion EDMs, which turns out to provide very powerful constraints.

[4] These interactions do not contribute to electroweak precision tests and Higgs production and decay at the dimension-six level.

Operator		Coupling
$-\sqrt{2}\varphi^\dagger\varphi\ \bar{q}_L\, Y'_u\, u_R\, \tilde{\varphi}$	O_Y	$y_t C_Y = [Y'_u]_{33}$
$-\frac{g_s}{\sqrt{2}}\ \bar{q}_L \sigma\cdot G\, \Gamma^u_g\, u_R\, \tilde{\varphi}$	O_g	$y_t C_g = [\Gamma^u_g]_{33}$
$-\frac{g'}{\sqrt{2}}\ \bar{q}_L \sigma\cdot B\, \Gamma^u_B\, u_R\, \tilde{\varphi}$	$O_{\gamma,Wt}$	$y_t Q_t C_\gamma = -[\Gamma^u_B + \Gamma^u_W]_{33}$
$-\frac{g}{\sqrt{2}}\ \bar{q}_L \sigma\cdot W^a\tau^a\, \Gamma^u_W\, u_R\, \tilde{\varphi}$		$y_t C_{Wt} = [\Gamma^u_W]_{33}$
$-\frac{g}{\sqrt{2}}\ \bar{q}_L \sigma\cdot W^a\tau^a\, \Gamma^d_W\, d_R\, \varphi$	O_{Wb}	$y_b C_{Wb} = [\Gamma^d_W]_{33}$

Table 1: High-scale operators in $SU(2)\times U(1)$ invariant form [53,54] (left column) and mapping to the operators and couplings used in this work (center and right column). q_L represents the L-handed quark doublet, φ is the Higgs doublet, and $\tilde{\varphi} = i\sigma_2\varphi^*$. g_s, g, g' denote the $SU(3)$, $SU(2)$, and $U(1)$ gauge couplings, $y_{t,b} = m_{t,b}/v$, and $\sigma\cdot X = \sigma_{\mu\nu}X^{\mu\nu}$. The couplings C_α are related to the 33 components of the matrices Y'_u and $\Gamma^{u,d}_{g,B,W}$ in the quark mass basis.

Having introduced all the operator structures relevant for our analysis, we discuss the renormalization group equations related to these operators in the next section.

3 The renormalization group equations

To connect the top-Higgs couplings to observables, Eq. (4) has to be evolved from the scale of new physics, Λ, to lower energies. For collider experiments the evolution to roughly the electroweak scale ($m_{t,h,Z}$) is sufficient, while for $b\to s\gamma$ measurements one has to lower the renormalization scale to $\mu\sim m_b$. Finally the connection to EDMs will involve the evolution down to the QCD scale, $\Lambda_\chi\sim 1$ GeV, where QCD becomes strongly coupled and non-perturbative techniques are required. An overview of the leading contributions to observables induced in this way is presented in Table 6 and 7.

The effects of lowering the energy scale on the real and imaginary parts of the top-Higgs couplings are determined by the renormalization group equations

$$\frac{d\,\mathrm{Re}\,\vec{C}_t}{d\ln\mu} = \gamma_t\cdot \mathrm{Re}\,\vec{C}_t, \qquad \frac{d\,\mathrm{Im}\,\vec{C}_t}{d\ln\mu} = \tilde{\gamma}_t\cdot \mathrm{Im}\,\vec{C}_t, \tag{6}$$

where $\vec{C}_t = (C_\gamma,\, C_g,\, C_{Wt},\, C_{Wb},\, C_Y)^T$. The relevant anomalous dimensions are given by [70–73]

$$\gamma_t = \frac{\alpha_s}{4\pi}\begin{pmatrix} 8C_F & -8C_F & \gamma_{Wt\to\gamma} & \gamma_{Wb\to\gamma} & 0\\ \gamma_{\gamma\to g} & 16C_F-4N_c & \gamma_{Wt\to g} & 0 & 0\\ 0 & 2C_F & 8C_F & 0 & 0\\ 0 & 0 & 0 & 8C_F & 0\\ 0 & 30C_F y_t^2 & 0 & 0 & 0 \end{pmatrix}, \tag{7}$$

$O_{\varphi G} = g_s^2 \varphi^\dagger \varphi G_{\mu\nu} G^{\mu\nu}$	$O_{\varphi \tilde{G}} = -g_s^2 \varphi^\dagger \varphi G_{\mu\nu} \tilde{G}^{\mu\nu}$
$O_{\varphi W} = g^2 \varphi^\dagger \varphi W^i_{\mu\nu} W^{i\mu\nu}$	$O_{\varphi \tilde{W}} = -g^2 \varphi^\dagger \varphi \tilde{W}^i_{\mu\nu} W^{i\mu\nu}$
$O_{\varphi B} = g'^2 \varphi^\dagger \varphi B_{\mu\nu} B^{\mu\nu}$	$O_{\varphi \tilde{B}} = -g'^2 \varphi^\dagger \varphi \tilde{B}_{\mu\nu} B^{\mu\nu}$
$O_{\varphi WB} = g g' \varphi^\dagger \tau^i \varphi W^i_{\mu\nu} B^{\mu\nu}$	$O_{\varphi \tilde{W} B} = -g g' \varphi^\dagger \tau^i \varphi \tilde{W}^i_{\mu\nu} B^{\mu\nu}$
$O^{(3)}_{lequ} = (\bar{l}^I_L \sigma^{\mu\nu} e_R) \epsilon_{IJ} (\bar{q}^J_L \sigma_{\mu\nu} u_R)$	
$O^{(1)}_{quqd} = (\bar{q}^I_L u_R) \epsilon_{IJ} (\bar{q}^J_L d_R)$,	$O^{(8)}_{quqd} = (\bar{q}^I_L \, t^a \, u_R) \epsilon_{IJ} (\bar{q}^J_L \, t^a \, d_R)$
$O_{\tilde{G}} = (1/6) g_s f_{abc} \epsilon^{\mu\nu\alpha\beta} G^a_{\alpha\beta} G^b_{\mu\rho} G^{c\ \rho}_{\nu}$	
$O^{(q)}_g = O_g\|_{t \to q} \qquad q = u, d, s$	
$O^{(bs)}_g = -(g_s/2)\, m_b\, \bar{s}_L \sigma_{\mu\nu} G^{\mu\nu} b_R\ (1 + h/v)$	
$O^{(f)}_\gamma = O_\gamma\|_{t \to f} \qquad f = e, u, d, s$	
$O^{(bs)}_\gamma = -(Q_b e/2)\, m_b\, \bar{s}_L \sigma_{\mu\nu}\, (F^{\mu\nu} - t_W Z^{\mu\nu})\, b_R\ (1 + h/v)$	

Table 2: Dimension-six operators induced by the top-Higgs interactions in Eq. (2) via RG flow and threshold corrections. We use the notation $\tilde{X}_{\mu\nu} \equiv \epsilon_{\mu\nu\alpha\beta} X^{\alpha\beta}/2$ and $\epsilon^{0123} = +1$. Below the electroweak scale the same operator basis and naming scheme can be used, by simply replacing $\varphi = (0,\, v + h)^T/\sqrt{2}$ and dropping terms involving the top quark, $Z^{\mu\nu}$, $W^{\mu\nu}$, and h.

where the electroweak contributions are given by

$$
\begin{aligned}
\gamma_{Wt\to\gamma} &= \frac{\alpha_w}{s_W^2 \alpha_s}\left[-4\left[1 + \frac{2T_t^3 Q_b}{Q_t}\frac{T_t^3 - 2s_W^2 Q_t}{c_W^2}\right] + \frac{2T_t^3}{Q_t}\left(\frac{m_t^2}{m_W^2} + 2\sum_{q=d,s,b} |V_{tq}|^2 \frac{m_q^2}{m_W^2}\right)\right], \\
\gamma_{Wb\to\gamma} &= \frac{\alpha_w}{s_W^2 \alpha_s}\frac{2T_t^3}{Q_t}\frac{m_b^2}{m_W^2}|V_{tb}|^2, \qquad \gamma_{Wt\to g} = \frac{\alpha_w}{\alpha_s}\frac{4}{s_W^2}\left(1 + 2T_t^3 \frac{T_t^3 - 2s_W^2 Q_t}{c_W^2}\right), \\
\gamma_{\gamma\to g} &= -\frac{\alpha_w}{\alpha_s} 8 Q_t \left(Q_t - \frac{T_t^3 - 2s_W^2 Q_t}{2c_W^2}\right).
\end{aligned}
\tag{8}
$$

The anomalous dimensions for the imaginary parts of the couplings, $\tilde{\gamma}_t$, are equivalent, with the replacement $30 \to 18$ in the $(5,2)$ element of Eq. (7) [5].

Although the above equations can be used to evolve the top-Higgs couplings from Λ to m_t, they are not sufficient to connect the top-Higgs couplings to experiment. In many cases important contributions arise from the inclusion of the additional operators of the previous section. To take these effects into account, we discuss how the additional operators are induced below, while a summary is presented in Tables 6 and 7.

[5] At one loop, the chromo-MDM and chromo-EDM operators induce, respectively, a correction to the top mass (and dimension-4 top Yukawa) and a top pseudoscalar mass. The pseudoscalar top quark mass term is not present in the effective Lagrangian of Eq. (4), and can be eliminated through an axial transformation of the quark field, with the net effect of changing the $(5,2)$ element of Eq. (7). For all the observables we consider, the modification of the running of the top mass is effectively a dimension-eight effect, and thus beyond our working accuracy.

3.1 RG equations for high-energy probes

The operators appearing in $\mathcal{L}_{\varphi\varphi XX}$ (Eq. (5a)) are induced through the one-loop RGEs,

$$\frac{d\vec{C}_{\varphi\varphi XX}}{d\ln\mu} = \gamma_{t\to\varphi\varphi XX}\cdot \mathrm{Re}\,\vec{C}_t \tag{9}$$

where $\vec{C}_{\varphi\varphi XX} = (C_{\varphi G},\, C_{\varphi B},\, C_{\varphi W},\, C_{\varphi WB})^T$ and the anomalous dimensions are given by [57, 74, 75],

$$\gamma_{t\to\varphi\varphi XX} = \frac{y_t^2 N_c}{(4\pi)^2}\begin{pmatrix} 0 & -C_F & 0 & 0 & 0 \\ 4Q_t(2Q_t - T_t^3) & 0 & 16Q_tT_t^3 - 2 & (16Q_bT_b^3 - 2)\left(\frac{y_b}{y_t}\right)^2 & 0 \\ 0 & 0 & -2 & -2\left(\frac{y_b}{y_t}\right)^2 & 0 \\ -4Q_tT_t^3 & 0 & 16Q_tT_t^3 - 4 & (16Q_bT_b^3 - 4)\left(\frac{y_b}{y_t}\right)^2 & 0 \end{pmatrix}. \tag{10}$$

Although $c_{Wb,\,Wt}$ do contribute to the Higgs-gauge operators, they do not induce the linear combination that contributes to $h\to\gamma\gamma$. Up to one-loop in QCD, these operators do not undergo self-renormalization.

3.2 RG equations for $b\to s\gamma$

The top-Higgs couplings contribute to $b\to s\gamma$ decays by inducing the flavor-violating operators of $\mathcal{L}_{b\to s}$ in Eq. (5c).

The evolution and mixing of these two operators among themselves is the same as for O_γ and O_g. In combination with the mixing with the top-Higgs couplings this gives rise to the following RGEs

$$\frac{d\vec{C}_{(bs)}}{d\ln\mu} = \gamma_{(bs)}\cdot\vec{C}_{(bs)} + \gamma_{t\to(bs)}\cdot\vec{C}_t, \tag{11}$$

with $\vec{C}_{(bs)} = (C_\gamma^{(bs)},\, C_g^{(bs)})^T$ and [23, 57, 76]

$$\begin{aligned} \gamma_{(bs)} &= \frac{\alpha_s}{4\pi}\begin{pmatrix} 8C_F & -8C_F \\ 0 & 16C_F - 4N_c \end{pmatrix}, \\ \gamma_{t\to(bs)} &= \frac{V_{tb}V_{ts}^*}{4\pi^2}y_t^2\begin{pmatrix} -\frac{1}{2}Q_t/Q_b & 0 & -1/Q_b & 2/Q_b & 0 \\ 0 & -\frac{1}{2} & 0 & 0 & 0 \end{pmatrix}. \end{aligned} \tag{12}$$

3.3 RG equations for EDMs

At low energies the experimental EDMs are determined by the quark (color-)EDMs, the Weinberg operator, and the electron EDM, collected in $\vec{C}_{\rm EDM} = (\tilde{c}_\gamma^{(q)},\, \tilde{c}_g^{(q)},\, C_{\tilde{G}},\, \tilde{c}_\gamma^{(e)})^T$. The top-Higgs couplings induce these Wilson coefficients in two ways; either directly, or by generating an additional set of Higgs-gauge couplings, $\vec{C}_{\varphi\varphi X\tilde{X}} = (C_{\varphi\tilde{G}},\, C_{\varphi\tilde{B}},\, C_{\varphi\tilde{W}},\, C_{\varphi\tilde{W}B})^T$, and four-fermion

operators, $\vec{C}_{\bar{L}R} = (C^{(3)}_{lequ}, C^{(1)}_{quqd}, C^{(8)}_{quqd})^T$, which in turn contribute to $\vec{C}_{\rm EDM}$. Including the self-renormalization of the operators in Eq. (5e), there are three relevant RG effects, described by the following RGEs,

$$\begin{aligned}\frac{d\vec{C}_{\rm EDM}}{d\ln\mu} &= \gamma_{\rm EDM}\cdot\vec{C}_{\rm EDM} + \gamma_{t\to\rm EDM}\cdot{\rm Im}\,\vec{C}_t \\ &\quad + \gamma_{\varphi\varphi X\tilde{X}\to\rm EDM}\cdot\vec{C}_{\varphi\varphi X\tilde{X}} + \gamma_{\bar{L}R\to\rm EDM}\cdot{\rm Im}\,\vec{C}_{\bar{L}R}. \end{aligned} \tag{13}$$

The first term in Eq. (13) describes the RG evolution of the quark (C)EDMs and Weinberg operator and the way they mix among themselves [77–79] (the electron EDM, $\tilde{c}^{(e)}_\gamma$ does not run up to one-loop in QCD),

$$\gamma_{\rm EDM} = \frac{\alpha_s}{4\pi}\begin{pmatrix} 8C_F & -8C_F & 0 & 0 \\ 0 & 16C_F - 4N_c & 2N_c & 0 \\ 0 & 0 & N_c + 2n_f + \beta_0 & 0 \\ 0 & 0 & 0 & 0 \end{pmatrix}. \tag{14}$$

The second term in Eq. (13) describes the direct contribution, while the third and fourth terms facilitate the two-step mechanism mentioned above. We briefly discuss these terms below.

3.3.1 Direct contribution

The second term in Eq. (13) represents the direct mixing of the top-Higgs interactions with the quark (color-)EDMs. The anomalous dimensions are given by [18], [6]

$$\gamma_{t\to\rm EDM} = \tag{15}$$
$$\frac{y_t^2}{(4\pi)^2}\begin{pmatrix} -2\frac{Q_t}{Q_q}|V_{tq}|^2\delta^q_{d,s,b} & 0 & 4\frac{2T^3_q}{Q_q}|V_{tq}|^2\delta^q_{d,s,b} & 4\frac{2T^3_q}{Q_q}|V_{qb}|^2\frac{y_b^2}{y_t^2}\delta^q_{u,c} & 0 \\ 0 & -2|V_{tq}|^2\delta^q_{d,s,b} & 0 & 16\frac{m_W^2}{m_t^2}\left[1 + 2T^3_b\frac{T^3_b - 2s^2_W Q_b}{c^2_W}\right]\delta^q_b & 0 \\ 0 & 0 & 0 & 0 & 0 \\ 0 & 0 & 0 & 0 & 0 \end{pmatrix}.$$

Note that the contributions to the light quark EDMs and CEDMs are always proportional to the combination of CKM elements, $|V_{td,ts,ub}|^2$, and there are no direct one-loop contributions to the electron EDM.

3.3.2 Two-step mechanism

The third and fourth terms in Eq. (13) are due to the two-step mechanism outlined above. There are two ways in which this mechanism can contribute to EDMs. In the first step, one induces the CP-odd Higgs-gauge interactions and four-fermion operators through the diagrams in the top panel of Fig. 1. In the second step these additional operators induce $\vec{C}_{\rm EDM}$ through the

[6] We neglected the contribution of $\tilde{c}_{Wb}$ to the b-quark EDM, because $\tilde{c}_{Wb}$ is mainly constrained through its contribution to the b-quark CEDM and the Weinberg operator.

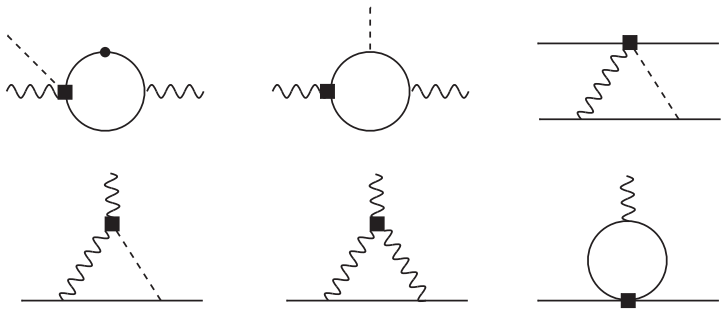

Figure 1: Representative diagrams contributing to the mixing of C_γ into $C_{\varphi\tilde{W},\varphi\tilde{B},\varphi\tilde{W}B,quqd,lequ}$ (top panel), and the mixing of the latter into light fermion electroweak dipoles (bottom panel). The square (circle) represents an operator (quark mass) insertion. Solid, wavy, and dotted lines represent fermions, electroweak gauge bosons, and the Higgs, respectively.

diagrams in the bottom panel of Fig. 1. We present the relevant anomalous dimensions for the two different paths, through the Higgs-gauge or four-fermion couplings, below.

Path 1: $\vec{C}_t \to \vec{C}_{\varphi\varphi X\tilde{X}} \to \vec{C}_{\rm EDM}$

In the first step of this path the CP-odd Higgs-gauge interactions are generated by the top-Higgs couplings in the same way as for their CP-even analogues,

$$\frac{d\vec{C}_{\varphi\varphi X\tilde{X}}}{d\ln\mu} = \gamma_{t\to\varphi\varphi X\tilde{X}} \cdot \mathrm{Im}\,\vec{C}_t, \qquad \gamma_{t\to\varphi\varphi X\tilde{X}} = \gamma_{t\to\varphi\varphi XX}, \tag{16}$$

where $\gamma_{t\to\varphi\varphi XX}$ is given in Eq. (10), while the Higgs-gauge interactions themselves do not run up to one-loop in QCD. [7]

In the second step, the Higgs-gauge operators generate the quark (color-)EDMs and electron EDM through the third term in Eq. (13). The anomalous dimensions are [57, 68]

$$\gamma_{\varphi\varphi X\tilde{X}\to\rm EDM} = \frac{\alpha_w}{4\pi}\begin{pmatrix} 0 & 4\frac{2Q_q-T_q^3}{Q_q c_W^2} & 4\frac{T_q^3}{Q_q s_W^2} & 2\frac{t_W^2(T_q^3-2Q_q)-3T_q^3}{Q_q s_W^2} \\ -8\frac{\alpha_s}{\alpha_w} & 0 & 0 & 0 \\ 0 & 0 & 0 & 0 \\ 0 & 4\frac{2Q_e-T_e^3}{Q_e c_W^2} & 4\frac{T_e^3}{Q_e s_W^2} & 2\frac{t_W^2(T_e^3-2Q_e)-3T_e^3}{Q_e s_W^2} \end{pmatrix}. \tag{17}$$

Path 2: $\vec{C}_t \to \vec{C}_{\bar{L}R} \to \vec{C}_{\rm EDM}$

The generation and evolution of the four-fermion operators of Eq. (5d) in the first step is determined by the additional RGEs,

$$\frac{d\vec{C}_{\bar{L}R}}{d\ln\mu} = \gamma_{\bar{L}R} \cdot \vec{C}_{\bar{L}R} + \gamma_{t\to\bar{L}R} \cdot \vec{C}_t, \tag{18}$$

[7] This is due to the fact that we include a factor of g_s^2 in the definition of the operators O_G and $O_{\tilde{G}}$. Moreover, we neglect self-renormalizations of $O(y_t^2)$ induced by the Higgs field wavefunction renormalization [55–57].

with $\vec{C}_{\bar{L}R} = (C^{(3)}_{lequ}, C^{(1)}_{quqd}, C^{(8)}_{quqd})^T$. The QCD self-renormalization is determined by,

$$\gamma_{\bar{L}R} = \frac{\alpha_s}{4\pi}\begin{pmatrix} 2C_F & 0 & 0 \\ 0 & -12C_F & \frac{4}{N_c}C_F \\ 0 & 8 & 4C_F \end{pmatrix}, \tag{19}$$

while the anomalous dimensions relevant for the mixing are given by

$$\gamma_{t\to\bar{L}R} = \frac{g^2 y_t}{(4\pi)^2}\begin{pmatrix} -y_e t_W^2 Q_t(2Q_e - T_e^3) & 0 & -y_e(\frac{3}{2} + t_W^2(2Q_e - T_e^3)) & 0 & 0 \\ \frac{8}{N_c} y_q Q_t(2Q_q - T_q^3) & -\frac{16}{N_c}\frac{g_s^2}{g^2} y_q C_F & \frac{8}{N_c} y_q(\frac{3}{2} + t_W^2(2Q_q - T_q^3)) & 0 & 0 \\ 16 y_q Q_t(2Q_q - T_q^3) & \frac{16}{N_c}\frac{g_s^2}{g^2} y_q & 16 y_q(\frac{3}{2} + t_W^2(2Q_q - T_q^3)) & 0 & 0 \end{pmatrix}. \tag{20}$$

where the terms with $q = d, s, b$, contribute to the four-quark operators, $O^{(1),(8)}_{q_i u_3 q_3 d_i}$, with $i = 1, 2, 3$, involving the first, second, or third generation down-type quarks, respectively. For example, the anomalous dimensions with $q = d$ generate the four-quark operators $O^{(1),(8)}_{quqd}$ with flavor structure $(\bar{u}_L t_R)(\bar{b}_L d_R) - (\bar{d}_L t_R)(\bar{t}_L d_R)$, while the flavor structure of the generated semi-leptonic operator of interest is $(\bar{\nu}_L t_R)(\bar{b}_L e_R) - (\bar{e}_L t_R)(\bar{t}_L e_R)$.

Finally, in the second step, the four-fermion operators generate the (C)EDMs of light quarks and the electron EDM through the following anomalous dimensions,

$$\gamma_{\bar{L}R\to\mathrm{EDM}} = \frac{1}{(4\pi)^2}\begin{pmatrix} 0 & 2\frac{Q_t y_t}{Q_q y_q} & 2C_F\frac{Q_t y_t}{Q_q y_q} \\ 0 & -2\frac{y_t}{y_q} & \frac{1}{N_c}\frac{y_t}{y_q} \\ 0 & 0 & 0 \\ -16N_c\frac{Q_t y_t}{Q_e y_e} & 0 & 0 \end{pmatrix}, \tag{21}$$

where the terms with $q = d, s, b$ correspond to the contributions from four-quark operators involving the first, second, and third generation to the down, strange, and bottom (C)EDMs, respectively.

3.4 RGE Summary

In summary, we can collect the Wilson coefficients of the extended operator basis in a single vector [8]

$$\vec{C} = (\mathrm{Re}\,\vec{C}_t, \mathrm{Im}\,\vec{C}_t, \vec{C}_{\varphi\varphi XX}, \vec{C}_{\varphi\varphi X\tilde{X}}, \mathrm{Im}\,\vec{C}_{\bar{L}R}, \mathrm{Re}\,\vec{C}_{(bs)}, \mathrm{Im}\,\vec{C}_{(bs)}, \vec{C}_{\mathrm{EDM}})^T \tag{22}$$

satisfying

$$\frac{d\vec{C}}{d\ln\mu} = \Gamma\cdot\vec{C}\ , \tag{23}$$

[8]The real parts of the four-fermion couplings, $\vec{C}_{\bar{L}R}$, are generated in the same way as their imaginary parts. However, since these do not contribute to EDMs, or any other sensitive observables, we neglect them in the basis, Eq. (22).

$\Lambda = 1\,\text{TeV}$	$c_\gamma(\Lambda)$	$c_g(\Lambda)$	$c_{Wt}(\Lambda)$	$c_{Wb}(\Lambda)$	$c_Y(\Lambda)$
$c_\gamma(m_t^+)$	0.86	0.13	$-9.2\cdot10^{-3}$	$-7.7\cdot10^{-6}$	–
$c_g(m_t^+)$	$2.8\cdot10^{-3}$	0.87	-0.021	$-1.2\cdot10^{-8}$	–
$c_{Wt}(m_t^+)$	$-5.4\cdot10^{-5}$	-0.033	0.86	–	–
$c_{Wb}(m_t^+)$	–	–	–	0.86	–
$c_Y(m_t^+)$	$-3.2\cdot10^{-4}$	-0.20	$2.4\cdot10^{-3}$	–	1
$C_{\varphi G}(m_t^+)$	$2.6\cdot10^{-5}$	$1.6\cdot10^{-2}$	$-2.0\cdot10^{-4}$	$-7.7\cdot10^{-11}$	–
$C_{\varphi\gamma}(m_t^+)$	$-4.2\cdot10^{-4}$	$-3.1\cdot10^{-5}$	$2.1\cdot10^{-6}$	$1.8\cdot10^{-9}$	–
$C_{\varphi WB}(m_t^+)$	$1.6\cdot10^{-2}$	$1.5\cdot10^{-3}$	$-1.6\cdot10^{-2}$	$5.5\cdot10^{-6}$	–

Table 3: The contributions of the operators in Eq. (3) at $\Lambda = 1$ TeV, to the operators relevant for high-energy probes at $\mu = m_t$. A dash, " – ", indicates no, or a negligible, contribution.

with

$$\Gamma = \begin{pmatrix} \gamma_t & - & - & - & - & - & - & - \\ - & \tilde{\gamma}_t & - & - & - & - & - & - \\ \gamma_{t\to\varphi\varphi XX} & - & - & - & - & - & - & - \\ - & \gamma_{t\to\varphi\varphi X\tilde{X}} & - & - & - & - & - & - \\ - & \gamma_{t\to\bar{L}R} & - & - & \gamma_{\bar{L}R} & - & - & - \\ \gamma_{t\to(bs)} & - & - & - & - & \gamma_{(bs)} & - & - \\ - & \gamma_{t\to(bs)} & - & - & - & - & \gamma_{(bs)} & - \\ - & \gamma_{t\to\text{EDM}} & - & \gamma_{\varphi\varphi X\tilde{X}\to\text{EDM}} & \gamma_{\bar{L}R\to\text{EDM}} & - & - & \gamma_{\text{EDM}} \end{pmatrix} \tag{24}$$

In our phenomenological analysis we will solve these RG equations with the initial condition at the high scale Λ given by $\vec{C}(\Lambda) = (\text{Re}\,\vec{C}_t(\Lambda),\, \text{Im}\,\vec{C}_t(\Lambda),\, 0,\, 0,\, 0,\, 0,\, 0,\, 0)^T$.

3.5 Evolution to $\mu = m_t$

As discussed above, for collider observables, it is mainly the mixing among the top-Higgs couplings themselves and the Higgs-gauge interactions, Eq. (5a), that is relevant. The RGEs of section 3.1 can be used to first run the couplings down to $\mu = m_t$, where the top-Higgs couplings are integrated out. To evaluate the RGEs, we employ input on the gauge couplings, W, Z, and quark masses, and CKM elements from Ref. [80]. In particular, we used the values of the quark masses in the $\overline{\text{MS}}$ scheme. The resulting Wilson coefficients, relevant for high-energy probes, are collected in Table 3.

Apart from the RG effects, additional threshold effects appear, as a result of integrating out

$\Lambda = 1\,\text{TeV}$	$C_\gamma(\Lambda)$	$C_g(\Lambda)$	$C_{Wt}(\Lambda)$	$C_{Wb}(\Lambda)$	$C_Y(\Lambda)$
$C_\gamma^{(bs)}(m_t^+)$	$6.2 \cdot 10^{-4}$	$-1.2 \cdot 10^{-5}$	$1.9 \cdot 10^{-3}$	$-3.7 \cdot 10^{-3}$	–
$C_g^{(bs)}(m_t^+)$	$-5.2 \cdot 10^{-7}$	$-3.2 \cdot 10^{-4}$	$3.9 \cdot 10^{-6}$	$1.5 \cdot 10^{-12}$	–
$C_\gamma^{(bs)}(\mu_b)$	$3.4 \cdot 10^{-4}$	$-1.2 \cdot 10^{-4}$	$1.0 \cdot 10^{-3}$	$-2.0 \cdot 10^{-3}$	–
$C_g^{(bs)}(\mu_b)$	$-3.0 \cdot 10^{-7}$	$-1.9 \cdot 10^{-4}$	$2.3 \cdot 10^{-6}$	$9.0 \cdot 10^{-13}$	–

Table 4: The contributions of the operators in Eq. (3) at $\Lambda = 1$ TeV, to the operators relevant for $b \to s\gamma$ transitions at $\mu = m_t$ and $\mu = \mu_b \approx 2$ GeV. A dash, " – ", indicates no, or a negligible, contribution.

the top-quark. At this scale, the top Yukawa induces contributions to the Higgs-gauge operators,

$$\begin{aligned} C_{\varphi G}(m_t^-) &= C_{\varphi G}(m_t^+) + \frac{1}{48\pi^2}\big(1 + c_Y(m_t^+)\big), \\ C_{\varphi\gamma}(m_t^-) &= C_{\varphi\gamma}(m_t^+) + \frac{1}{4\pi^2}\left[\frac{N_c Q_t^2}{6}\big(1 + c_Y(m_t^+)\big) - \frac{21}{24}A(\tau_W)\right], \\ A(\tau) &= \frac{1}{7}\left(2 + 3\tau + 3\tau(2-\tau)\arcsin\left(\frac{1}{\sqrt{\tau}}\right)^2\right), \qquad \tau_W = 4\frac{m_W^2}{m_h^2}, \end{aligned} \tag{25}$$

where the constant terms arise from the SM top and $W^\pm$ loops, while $C_{\varphi\gamma}$ represents the coupling of $e^2 v h F_{\mu\nu}F^{\mu\nu}$, which corresponds to the linear combination $C_{\varphi B} + C_{\varphi W} - C_{\varphi WB}$.

3.6 Evolution to $\mu = \mu_b$

For the $b \to s\gamma$ observables, the main contributions follow from the mixing onto the flavor-violating operators, $O_{\gamma,g}^{(bs)}$. In this case we employ the RGEs of section 3.2, to run to the scale $\mu = m_t$. Below this threshold the top-Higgs operators are integrated out, such that the top-Higgs couplings no longer contribute below this scale. The operators $O_{\gamma,g}^{(bs)}$ can then straightforwardly be evolved down to $\mu = \mu_b$ by use of the same RGEs with the mixing terms set to zero, $\gamma_{t\to(bs)} \to 0$. As we will employ expressions for the $b \to s\gamma$ observables in terms of the couplings at $\mu = m_t$ and $\mu = \mu_b$, we present the values of $C_{\gamma,g}^{(bs)}$ at both scales in Table 4.

3.7 Evolution to $\mu = \Lambda_\chi$

Evaluating the contributions to EDMs is somewhat more involved. At low energies, around Λ_χ, the light-quark (C)EDMs, the Weinberg operator, and the electron EDM contribute to EDMs, while the charm- and bottom-quark CEDMs facilitate indirect contributions. As a result, the mixing of the original top-Higgs operators in Eq. (2) with the additional operators in Eq. (5e) determines the contribution to EDMs. Apart from the mixing, the matching corrections at the different thresholds are relevant as well.

First the RGE of Eq. (13) is used to run the operators from $\mu = \Lambda$ to $\mu = m_t$, where we integrate out the top quark and the Higgs boson. This implies that the top-Higgs and the additional Higgs-gauge couplings and their corresponding operators are removed from the EFT below $\mu = m_t$. This gives rise to several threshold corrections to the operators in Eq. (5e). The Yukawa interaction, $\tilde{c}_Y$, contributes to the (C)EDMs [81–85] and the Weinberg operator [77,86]

$\Lambda = 1\,\text{TeV}$	$\tilde{c}_\gamma(\Lambda)$	$\tilde{c}_g(\Lambda)$	$\tilde{c}_{Wt}(\Lambda)$	$\tilde{c}_{Wb}(\Lambda)$	$\tilde{c}_Y(\Lambda)$
$\tilde{c}_\gamma^{(e)}(\Lambda_\chi)$	$3.8 \cdot 10^{-4}$	$1.4 \cdot 10^{-5}$	$-4.4 \cdot 10^{-4}$	$2.3 \cdot 10^{-8}$	$4.0 \cdot 10^{-5}$
$\tilde{c}_\gamma^{(u)}(\Lambda_\chi)$	$1.4 \cdot 10^{-4}$	$6.3 \cdot 10^{-4}$	$-1.2 \cdot 10^{-4}$	$-2.9 \cdot 10^{-6}$	$-6.1 \cdot 10^{-5}$
$\tilde{c}_g^{(u)}(\Lambda_\chi)$	$3.9 \cdot 10^{-6}$	$1.1 \cdot 10^{-3}$	$-1.9 \cdot 10^{-5}$	$-1.7 \cdot 10^{-5}$	$-1.0 \cdot 10^{-4}$
$\tilde{c}_\gamma^{(d)}(\Lambda_\chi)$	$2.0 \cdot 10^{-4}$	$8.6 \cdot 10^{-4}$	$-9.1 \cdot 10^{-4}$	$-2.9 \cdot 10^{-6}$	$-6.1 \cdot 10^{-5}$
$\tilde{c}_g^{(d)}(\Lambda_\chi)$	$2.9 \cdot 10^{-6}$	$1.3 \cdot 10^{-3}$	$-2.4 \cdot 10^{-5}$	$-1.7 \cdot 10^{-5}$	$-1.0 \cdot 10^{-4}$
$\tilde{c}_\gamma^{(s)}(\Lambda_\chi)$	$1.9 \cdot 10^{-4}$	$8.6 \cdot 10^{-4}$	$-9.5 \cdot 10^{-4}$	$-2.9 \cdot 10^{-6}$	$-6.1 \cdot 10^{-5}$
$\tilde{c}_g^{(s)}(\Lambda_\chi)$	$2.9 \cdot 10^{-6}$	$1.3 \cdot 10^{-3}$	$-2.4 \cdot 10^{-5}$	$-1.7 \cdot 10^{-5}$	$-1.0 \cdot 10^{-4}$
$C_{\tilde{G}}(\Lambda_\chi)$	$-2.8 \cdot 10^{-6}$	$-8.8 \cdot 10^{-4}$	$2.2 \cdot 10^{-5}$	$7.8 \cdot 10^{-5}$	$-8.1 \cdot 10^{-7}$

Table 5: The contributions of the operators in Eq. (3) at $\Lambda = 1$ TeV, to the operators relevant for EDMs at $\mu = \Lambda_\chi$.

through Barr-Zee diagrams, while the top CEDM gives rise to a one-loop threshold contribution to the Weinberg operator [79, 87]. In total we have the following matching conditions,

$$\begin{aligned}
\tilde{c}_\gamma^{(f)}(m_t^-) &= \tilde{c}_\gamma^{(f)}(m_t^+) + 24\frac{\alpha}{(4\pi)^3}Q_t^2 f(x_t)\tilde{c}_Y(m_t^+), \\
\tilde{c}_g^{(q)}(m_t^-) &= \tilde{c}_g^{(q)}(m_t^+) - 4\frac{\alpha_s}{(4\pi)^3}f(x_t)\tilde{c}_Y(m_t^+), \\
C_{\tilde{G}}(m_t^-) &= C_{\tilde{G}}(m_t^+) - \frac{\alpha_s}{8\pi}\tilde{c}_g(m_t^+) - 4\frac{\alpha_s}{(4\pi)^3}h(m_t, m_h)\,\tilde{c}_Y(m_t^+),
\end{aligned} \tag{26}$$

where m_t^+ (m_t^-) indicates a scale just above (below) m_t, $x_t \equiv \frac{m_t^2}{m_h^2}$, and the functions f, and h are given by,

$$f(z) \equiv \tfrac{z}{2}\int_0^1 dx \tfrac{1-2x(1-x)}{x(1-x)-z}\ln\tfrac{x(1-x)}{z}\ , \qquad h(m,M) = \tfrac{m^4}{4}\int_0^1 dx\int_0^1 du \tfrac{u^3x^3(1-x)}{[m^2x(1-ux)+M^2(1-u)(1-x)]^2}\ .$$

Below $\mu = m_t$, our basis consists of the operators in Eq. (5e). The anomalous dimensions in Eq. (14) control the running down to $\mu = m_b$ and subsequently to $\mu = m_c$. At these thresholds the bottom and charm quarks and their (C)EDMs are integrated out, which results in additional threshold corrections to the Weinberg operator,

$$C_{\tilde{G}}(m_{c,b}^-) = C_{\tilde{G}}(m_{c,b}^+) - \frac{\alpha_s}{8\pi}\tilde{c}_g^{(c,b)}(m_{c,b}^+). \tag{27}$$

After the charm threshold the remaining operators can be evolved to Λ_χ using Eq. (14). The numerical result of this analysis is presented in Table 5 for $\Lambda = 1$ TeV.

An overview of the effects of the running and threshold contributions to observables presented in Table 6 for c_α and in Table 7 for $\tilde{c}_\alpha$.

	Obs.	c_γ	c_g	c_{Wt}	c_{Wb}	c_Y
Direct	t	✗	✗	✓	✗	✗
	$t\bar{t}$	✗	✓	✗	✗	✗
	$t\bar{t}h$	✗	✓	✗	✗	✓
	F_0, F_L, δ^-	✗	✗	✓	✗	✗
Indirect	$gg \leftrightarrow h$	✗	$\gamma^{(1,2)}_{t\to\varphi\varphi XX}$	✗	✗	**Threshold** (25)
	$h \to \gamma\gamma$	$\gamma^{(2,1),\,(4,1)}_{t\to\varphi\varphi XX}$	✗	✗	✗	**Threshold** (25)
S	S	$\gamma^{(4,1)}_{t\to\varphi\varphi XX}$	✗	$\gamma^{(4,3)}_{t\to\varphi\varphi XX}$	✗	✗
$\boldsymbol{b\to s\gamma}$	BR, A_{CP}	$\gamma^{(1,1)}_{t\to(bs)}$	✗	$\gamma^{(1,3)}_{t\to(bs)}$	$\gamma^{(1,4)}_{t\to(bs)}$	✗

Table 6: An overview of the dominant contributions of the real parts of the anomalous top-Higgs couplings to high- and low-energy observables. ✓ indicates a direct (tree-level) contribution, ✗ a negligible contribution, $\gamma_{t\to X}$ a contribution induced by the RG flow, and **Threshold** a threshold contribution with the appearing numbers indicating the corresponding equations.

	Obs.	$\tilde{c}_\gamma$	$\tilde{c}_g$	$\tilde{c}_{Wt}$	$\tilde{c}_{Wb}$	$\tilde{c}_Y$
Direct	t	✗	✗	✗	✗	✗
	$t\bar{t}$	✗	✗	✗	✗	✗
	$t\bar{t}h$	✗	✗	✗	✗	✗
	F_0, F_L, δ^-	✗	✗	✓	✗	✗
$\boldsymbol{b \to s\gamma}$	BR, A_{CP}	$\gamma^{(1,1)}_{t\to(bs)}$	✗	$\gamma^{(1,3)}_{t\to(bs)}$	$\gamma^{(1,4)}_{t\to(bs)}$	✗
EDMs	$d_{\rm ThO}$	$\gamma^{(i,1)}_{t\to\varphi\varphi X\tilde{X},\bar{L}R}\gamma^{(4,i)}_{\varphi\varphi X\tilde{X},\bar{L}R\to\rm EDM}$	$\gamma^{(1,2)}_t\gamma^{(i,1)}_{t\to\varphi\varphi X\tilde{X},\bar{L}R}\gamma^{(4,i)}_{\varphi\varphi X\tilde{X},\bar{L}R\to\rm EDM}$ $\gamma^{(3,2)}_t\gamma^{(i,3)}_{t\to\varphi\varphi X\tilde{X},\bar{L}R}\gamma^{(4,i)}_{\varphi\varphi X\tilde{X},\bar{L}R\to\rm EDM}$	$\gamma^{(i,3)}_{t\to\varphi\varphi X\tilde{X},\bar{L}R}\gamma^{(4,i)}_{\varphi\varphi X\tilde{X},\bar{L}R\to\rm EDM}$	✗	**Threshold** (26)
	d_n, $d_{\rm Hg}$	$\gamma^{(i,1)}_{t\to\varphi\varphi X\tilde{X},\bar{L}R}\gamma^{(1-3,i)}_{\varphi\varphi X\tilde{X},\bar{L}R\to\rm EDM}$	**Threshold** (26)	$\gamma^{(i,3)}_{t\to\varphi\varphi X\tilde{X},\bar{L}R}\gamma^{(1-3,i)}_{\varphi\varphi X\tilde{X},\bar{L}R\to\rm EDM}$	$\gamma^{(2,4)}_{t\to\rm EDM}$, **Threshold** (27)	**Threshold** (26)

Table 7: Similar to Table 6 but now for the imaginary parts of the anomalous top-Higgs couplings. Contributions that are generated at the two- or three-loop level are represented by entries involving a combination of anomalous dimensions and/or threshold contributions. For example, the leading contribution of $\tilde{c}_{Wb}$ to the mercury and neutron EDMs is due to the b-quark CEDM, $\tilde{c}_g^{(b)}$, which is RG-induced through $\gamma^{(2,4)}_{t\to\rm EDM}$ (Eq. (15)) and subsequently generates the Weinberg operator, $C_{\tilde{G}}$, through the threshold contribution of (27).

4 Collider constraints

In this section we discuss the constraints that collider experiments set on the top couplings introduced in Eq. (2). The top quark was discovered at the Tevatron [1, 2] and is abundantly produced at the LHC. This makes it possible to directly probe the properties of the top quark by measuring the cross sections of processes with top final states, and the subsequent top decays. In the former category, we consider single top, $t\bar{t}$, and associated Higgs $t\bar{t}$ production cross sections that are sensitive to anomalous top-gluon (O_g), top-W (O_{Wt} and O_{Wb}), and top-Higgs (O_Y) couplings. In the latter category we study the helicity fractions of W bosons that are produced in top quark decays. These fractions are sensitive to the top-bottom-W operators, O_{Wt} and, to a lesser extent, O_{Wb}. In addition to its contribution to single top production, the operator O_{Wb} generates a dipole coupling of the Z boson to $b\bar{b}$ pairs. This coupling affect the branching ratio $Z \to b\bar{b}$, which was precisely measured at LEP. Since the bounds turn out to be weak, we do not further discuss this observable.

The couplings of the top can be probed indirectly, by studying observables that do not have a top quark in the final state, but instead receive sizable corrections from top loops. We consider corrections to precision EW observables, in particular the S parameter [88–90], and the Higgs boson production and decay signal strengths. In the SM, the main Higgs production mechanism is gluon fusion and proceeds through a top loop. This process is therefore quite sensitive to modifications of the top Yukawa, C_Y, and to the top chromo-dipole moment C_g. In a similar way, the SM decay process $h \to \gamma\gamma$ is loop induced, and can be used to constrain C_Y and C_γ. We do not include corrections to Higgs production and decay mechanisms that are tree level in the SM, like vector boson fusion (VBF), $h \to WW^*$, or $h \to b\bar{b}$. Contributions to these processes from the operators in Eq. (2) are loop suppressed such that any resulting constraints are weak and can be neglected.

Finally we comment on the contributions from the anomalous couplings that we include. Our EFT approach is based on an expansion in Q/Λ where Q is a low-energy scale that can be identified with the typical energy in a process, the Higgs vev, or the mass of a SM particle. We always present our results as functions of the dimensionless combinations $v^2 C_\alpha$. In principle, the most important contributions are linear in this combination and appear at the dimension-six level, $\sim \mathcal{O}(1/\Lambda^2)$. However, this is not always the case. For instance, it might be that the interference terms are suppressed by small SM parameters (such as light fermion masses) or for kinematical reasons, such that the dimension-eight contributions (from the square of the dimension-six operators) can provide the dominant contribution. This is more likely if the bounds on the Wilson coefficients of the dimension-six operators are loose. A much more detailed discussion on dimension-eight effects in the framework of the SM EFT is given in Refs. [91–93]. That being said, we find that the bounds on the dimension-six coefficient are strong enough that dimension-eight contributions can be neglected. As such, we truncate the expansion at $\mathcal{O}(1/\Lambda^2)$ and do not consider terms that depend quadratically on $v^2 C_\alpha$. This means for example that for most of the collider observables under investigation, the imaginary parts of the Wilson coefficients do not contribute.

In the expressions below, we nevertheless provide various contributions proportional to the square of dimension-six operators. We will use these terms mainly as a diagnostic tool to check whether their impact can indeed be neglected. We stress that the dimension-eight contributions given below are not complete. In the cross sections and branching ratios we include dimension-eight effects from two insertions of the operators C_α in tree-level diagrams, but never consider

process	$\sqrt{S}$ (TeV)	σ (pb)			Experiment	
$t\bar{t}$	1.96	7.6 ± 0.4			CDF, D0	[94]
	8	242 ± 10			ATLAS	[95]
		239 ± 13			CMS	[96]
process	$\sqrt{S}$ (TeV)	t	$\bar{t}$	$t + \bar{t}$	Experiment	
single top	7	46 ± 6	23 ± 3	68 ± 8	ATLAS	[97]
t-channel		–	–	67 ± 7	CMS	[98]
	8	–	–	83 ± 12	ATLAS	[99]
		54 ± 5	28 ± 4	84 ± 8	CMS	[100]
	13	133 ± 26	96 ± 24	229 ± 48	ATLAS	[101]
		142 ± 23	81 ± 15	228 ± 34	CMS	[102]

Table 8: $t\bar{t}$ and single top total cross sections, measured at CDF, D0, ATLAS and CMS.

the insertion of genuine dimension-eight operators, or the mixing of two dimension-six operators onto dimension-eight operators.

4.1 Direct constraints

4.1.1 $t\bar{t}$ production

The cross section induced by the top chromo-magnetic dipole moment (CMDM), c_g, and CEDM, $\tilde{c}_g$, was computed in Refs. [103, 104] and is given by

$$\begin{aligned} \frac{\sigma_{t\bar{t}}(1.96\,\text{TeV})}{\text{pb}} &= (7.45 \pm 0.44) - (10.8 \pm 0.6)(v^2 c_g) + (7.1 \pm 0.7)(v^2 c_g)^2 + (2.5 \pm 0.5)(v^2 \tilde{c}_g)^2 \\ \frac{\sigma_{t\bar{t}}(8\,\text{TeV})}{\text{pb}} &= (252.9 \pm 20) - (333 \pm 28)\left(v^2 c_g\right) + (476 \pm 44)\left(v^2 c_g\right)^2 + (336 \pm 33)\left(v^2 \tilde{c}_g\right)^2 . \end{aligned} \tag{28}$$

The SM $t\bar{t}$ cross section has been computed using the program TOP++ [105]. It includes next-to-next-to-leading order (N^{2}LO) corrections [106] and soft gluon resummation. The cross section and the couplings c_g and $\tilde{c}_g$ are evaluated at the renormalization scale $\mu = m_t$. The theoretical uncertainties on the SM cross section arises from PDF and scale variations. As the contribution of C_g is only included at LO, the theoretical errors on terms proportional to c_g and $\tilde{c}_g$ in Eq. (28) only include PDF and α_s uncertainties, which are obtained by following the recipe of the PDF4LHC working group [107] with the three PDF sets CT10 [108], MSTW08 [109], and NNPDF2.3 [110]. In the SM, NLO and N^{2}LO corrections to the $t\bar{t}$ cross section are large [106] suggesting the need to include NLO corrections for the dipole operators as well [111]. We have not included these corrections here.

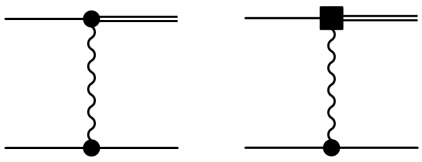

Figure 2: Contribution of C_{Wt} and C_{Wb} to t-channel single top production. Solid lines denote light quarks, double lines the top quark, and wavy lines the W boson. SM vertices are denoted by a dot, while an insertion of a C_{Wt} or C_{Wb} by a square.

Our fits include data from the Tevatron experiments [94] at $\sqrt{S} = 1.96$ TeV and from the ATLAS and CMS experiments at $\sqrt{S} = 8$ TeV [95,96]. The experimental results are summarized in Tab. 8.

4.1.2 Associated production of a Higgs boson and a $t\bar{t}$ pair

The $t\bar{t}h$ cross section receives contributions from the anomalous Yukawa coupling, C_Y, and from the dipole operator, C_g. In Ref. [51] we presented the $t\bar{t}h$ cross section induced by $\tilde{c}_g$ and $\tilde{c}_Y$ at LO in QCD. Here we extend the calculation with contributions from the real part of the couplings, c_Y and c_g, which interfere with the SM and induce genuine $\mathcal{O}(1/\Lambda^2)$ effects. The $t\bar{t}h$ cross section in the SM is known at NLO in QCD [112–115]. The contribution of the pseudoscalar Yukawa couplings is also known at NLO [116], while the effects of C_g has been considered at tree level in Refs. [117, 118]. Our results agree with Refs. [117, 118].

The observable we study is the ratio, $\mu_{t\bar{t}h}$, of the production cross section with and without dimension-six operators,

$$\mu_{t\bar{t}h} = \frac{\sigma_{pp\to t\bar{t}h}}{\sigma^{SM}_{pp\to t\bar{t}h}}. \tag{29}$$

At center-of-mass energy of 8 and 14 TeV, we find

$$\begin{aligned}
\mu_{t\bar{t}h}(8\,\text{TeV}) &= \left(1 + v^2 c_Y\right)^2 + (0.33 \pm 0.02)(v^2\tilde{c}_Y)^2 - (7.11 \pm 0.02)(v^2 c_g) \\
&\quad +(52 \pm 5)(v^2 c_g)^2 + (44 \pm 4)(v^2\tilde{c}_g)^2 \\
&\quad -(11.0 \pm 0.1)\left(v^2 c_g\right)(v^2 c_Y) - (0.12 \pm 0.16)\left(v^2\tilde{c}_g\right)(v^2\tilde{c}_Y) \\
\mu_{t\bar{t}h}(14\,\text{TeV}) &= \left(1 + v^2 c_Y\right)^2 + (0.42 \pm 0.01)(v^2\tilde{c}_Y)^2 - (7.57 \pm 0.03)\left(v^2 c_g\right) \\
&\quad +(80 \pm 5)\left(v^2 c_g\right)^2 + (72 \pm 5)\left(v^2\tilde{c}_g\right)^2 \\
&\quad -(11.5 \pm 0.1)\left(v^2 c_g\right)(v^2 c_Y) - (0.79 \pm 0.06)\left(v^2\tilde{c}_g\right)(v^2\tilde{c}_Y).
\end{aligned} \tag{30}$$

The theoretical error only includes PDF and α_s variations. The cross section, and the couplings C_Y and C_g, are evaluated at the scale $\mu = m_t$. The ATLAS and CMS measurements of the signal strength $\mu_{t\bar{t}h}$ are given in Table 11.

4.1.3 Single top production

The weak dipole operators C_{Wt} and C_{Wb} provide tree-level corrections to single top production cross sections and to the $t \to Wb$ decay.

The largest SM contribution to single top production is through the t-channel exchange of a W boson. Smaller contributions arise from the associated production of a top and a W boson and by s-channel W exchange. Production via the t-channel was first observed at the Tevatron [119,120]. ATLAS published the measurement of the inclusive and differential cross section at $\sqrt{S} = 7$ TeV with luminosity of 5 fb^{-1} [97], and preliminary results at $\sqrt{S} = 8$ and 13 TeV, with luminosity of, respectively, 20 fb^{-1} and 3.2 fb^{-1} , are also available [99, 101]. CMS published results at $\sqrt{S} = 7$ and $\sqrt{S} = 8$ TeV with luminosity of 1.56 and 20 fb^{-1}, respectively [98,100]. Preliminary results at $\sqrt{S} = 13$ TeV are given in Ref. [102]. The associated production of a top and a W boson has also been observed by both ATLAS and CMS [121,122], while the first observation of s-channel single top production has been recently announced by the Tevatron experiments [123]. In our analysis, we include only t-channel production, which gives the strongest bounds at the moment.

The total and differential SM cross sections are known at NLO in QCD [124–127], both in the 5 flavor scheme, in which the b quark is considered massless and appears in the initial state, and in the 4 flavor scheme, which keeps into account m_b effects. A detailed comparison of the two schemes is discussed in Ref. [127]. We computed the corrections of the operators C_{Wt} and C_{Wb} to the t-channel single top cross section in the 5 flavor scheme, including NLO QCD effects. The tree-level diagrams are displayed in Fig. 2. c_{Wt} interferes with the SM through terms proportional to m_t and contributes to the total cross section at $\mathcal{O}(1/\Lambda^2)$. The interference of c_{Wb} with the SM is proportional to m_b and vanishes in the 5 flavor scheme. The imaginary couplings $\tilde{c}_{Wt}$ and $\tilde{c}_{Wb}$ only contribute to the total cross section at $\mathcal{O}(1/\Lambda^4)$.

At NLO in QCD, the inclusive t-channel single top cross section in the presence of the operator C_{Wt} is

$$\begin{aligned}
\frac{\sigma_t(7\text{ TeV})}{\text{pb}} &= (41.9 \pm 1.8) - (9.4 \pm 0.3)\ v^2 c_{Wt} + (15.6 \pm 0.2)\,((v^2 c_{Wt})^2 + (v^2 \tilde{c}_{Wt})^2)\ , \\
\frac{\sigma_{\bar{t}}(7\text{ TeV})}{\text{pb}} &= (22.7 \pm 1.0) - (0.3 \pm 0.1)\, v^2 c_{Wt} + (5.5 \pm 0.2)\,((v^2 c_{Wt})^2 + (v^2 \tilde{c}_{Wt})^2)\ , \\
\frac{\sigma_t(8\text{ TeV})}{\text{pb}} &= (56.4 \pm 2.4) - (11.7 \pm 0.3)\ v^2 c_{Wt} + (21.0 \pm 0.5)\,((v^2 c_{Wt})^2 + (v^2 \tilde{c}_{Wt})^2)\ , \\
\frac{\sigma_{\bar{t}}(8\text{ TeV})}{\text{pb}} &= (30.7 \pm 1.3) - (0.5 \pm 0.2)\ v^2 c_{Wt} + (7.7 \pm 0.2)\,((v^2 c_{Wt})^2 + (v^2 \tilde{c}_{Wt})^2)\ , \\
\frac{\sigma_t(13\text{ TeV})}{\text{pb}} &= (136\ \ \pm 5.4) - (26.2 \pm 0.4)\ v^2 c_{Wt} + (57.0 \pm 1.0)\,((v^2 c_{Wt})^2 + (v^2 \tilde{c}_{Wt})^2)\ , \\
\frac{\sigma_{\bar{t}}(13\text{ TeV})}{\text{pb}} &= (81.0 \pm 4.1) - (2.6 \pm 0.4)\ v^2 c_{Wt} + (24.7 \pm 1.0)\,((v^2 c_{Wt})^2 + (v^2 \tilde{c}_{Wt})^2)\ .
\end{aligned} \tag{31}$$

The cross sections were obtained by setting the factorization and renormalization scales to $\mu = m_t$. The couplings c_{Wt} and $\tilde{c}_{Wt}$ are also evaluated at this scale and are related to the couplings at $\mu = \Lambda$ by the RGE discussed in Sec. 3.1. The scale uncertainty was estimated by varying the factorization and renormalization scales between $\mu = m_t/2$ and $\mu = 2m_t$. In the evaluation of the scale uncertainties, we accounted for the running of C_{Wt} between the central scale and $\mu = m_t/2$ or $\mu = 2m_t$. We obtained the PDF and α_s uncertainties following the PDF4LHC recipe, using the three PDF sets CT10 [108], MSTW08 [109] and NNPDF2.3 [110]. PDF uncertainties turn out to dominate the theoretical uncertainty. Corrections to the single top

	$d\sigma(t)/dp_T$ (10^{-3} pb/GeV)			
bins (GeV)	exp.	theory		
0-45	440 ± 65	(373 ± 22)	$-(71 \pm 5)\, v^2 c_{Wt}$	$+(48 \pm 4)\, ((v^2 c_{Wt})^2 + (v^2 \tilde{c}_{Wt})^2)$
45-75	370 ± 56	(382 ± 15)	$-(85 \pm 1)\, v^2 c_{Wt}$	$+(96 \pm 7)\, ((v^2 c_{Wt})^2 + (v^2 \tilde{c}_{Wt})^2)$
75-110	250 ± 37	(207 ± 8)	$-(52 \pm 5)\, v^2 c_{Wt}$	$+(87 \pm 4)\, ((v^2 c_{Wt})^2 + (v^2 \tilde{c}_{Wt})^2)$
110-150	133 ± 26	(90 ± 3)	$-(26 \pm 4)\, v^2 c_{Wt}$	$+(66 \pm 2)\, ((v^2 c_{Wt})^2 + (v^2 \tilde{c}_{Wt})^2)$
150-500	7.8 ± 1.4	(7.7 ± 0.4)	$-(2.2 \pm 0.5)\, v^2 c_{Wt}$	$+(13 \pm 1)\, ((v^2 c_{Wt})^2 + (v^2 \tilde{c}_{Wt})^2)$
	$d\sigma(\bar{t})/dp_T$ (10^{-3} pb/GeV)			
bins (GeV)	exp.	theory		
0-45	190 ± 52	(210 ± 14)	$-(10.2 \pm 4.7)\, v^2 c_{Wt}$	$+(14 \pm 2)\, ((v^2 c_{Wt})^2 + (v^2 \tilde{c}_{Wt})^2)$
45-75	230 ± 43	(202 ± 10)	$-(4.7 \pm 1.3)\, v^2 c_{Wt}$	$+(33 \pm 3)\, ((v^2 c_{Wt})^2 + (v^2 \tilde{c}_{Wt})^2)$
75-110	97 ± 26	(102 ± 4)	$+(0.7 \pm 4.7)\, v^2 c_{Wt}$	$+(34 \pm 2)\, ((v^2 c_{Wt})^2 + (v^2 \tilde{c}_{Wt})^2)$
110-150	13 ± 9	(42 ± 2)	$+(2.7 \pm 1.3)\, v^2 c_{Wt}$	$+(25 \pm 1)\, ((v^2 c_{Wt})^2 + (v^2 \tilde{c}_{Wt})^2)$
150-500	1.4 ± 0.8	(3.2 ± 0.2)	$+(0.4 \pm 0.2)\, v^2 c_{Wt}$	$+(5.0 \pm 0.2)\, ((v^2 c_{Wt})^2 + (v^2 \tilde{c}_{Wt})^2)$

Table 9: Single top differential cross section induced by C_{Wt} at $\sqrt{S} = 7$ TeV.

cross section from C_{Wt} and C_{Wb} have been considered in Ref. [128] at LO, and, recently, the NLO QCD corrections have been included [129]. Our results are in agreement with Refs. [128, 129].

In Table 9 we give the differential cross section $d\sigma/dp_T$, where p_T is the t or $\bar{t}$ transverse momentum, in the p_T bins relevant to the analysis of Ref. [97]. The different p_T bins are correlated and we included the experimental correlations given in Ref. [97] when constructing the χ^2. We neglected any correlations of theoretical uncertainties.

The contribution of C_{Wb} to single top production is suppressed by the factor of m_b appearing in the definition of the operator. We find

$$\begin{aligned}
(\sigma_t + \sigma_{\bar{t}})(7\,\text{TeV}) &= (0.11 \pm 0.01)\left((v^2 c_{Wb})^2 + (v^2 \tilde{c}_{Wb})^2\right)\ \text{pb}\ , \\
(\sigma_t + \sigma_{\bar{t}})(8\,\text{TeV}) &= (0.15 \pm 0.01)\left((v^2 c_{Wb})^2 + (v^2 \tilde{c}_{Wb})^2\right)\ \text{pb}\ , \\
(\sigma_t + \sigma_{\bar{t}})(13\,\text{TeV}) &= (0.44 \pm 0.01)\left((v^2 c_{Wb})^2 + (v^2 \tilde{c}_{Wb})^2\right)\ \text{pb}\ . \qquad (32)
\end{aligned}$$

In the 5 flavor scheme, C_{Wb} does not interfere with the SM, since the b quark in the initial state is taken to be massless. We do not expect the interference to be significantly larger than the terms in Eq. (32). These results imply that the single top cross section is sensitive to $v^2 C_{Wb} \sim \mathcal{O}(10)$. Such large values of $v^2 C_{Wb}$ are forbidden by flavor processes such as $b \to s\gamma$. For this reason, we do not include Eq. (32) in our analysis.

F_0	F_L	F_R	δ_-/π	experiment	
0.72 ± 0.08	0.31 ± 0.09	-0.03 ± 0.04	–	CDF & D0	[130]
0.67 ± 0.07	0.32 ± 0.04	0.01 ± 0.04	–	ATLAS	[131]
0.68 ± 0.04	0.31 ± 0.03	0.01 ± 0.01	–	CMS	[132]
0.72 ± 0.06	0.30 ± 0.04	-0.02 ± 0.02	–	CMS	[133]
–	0.37 ± 0.07 - F_R	–	-0.014 ± 0.036	ATLAS	[58]

Table 10: W helicity fractions measured at CDF, D0, ATLAS, and CMS.

4.1.4 W helicity fractions

The helicity fractions of W bosons produced from top quark decays are sensitive to the operator C_{Wt} and, to a lesser extent, C_{Wb}. We consider three helicity fractions: F_0, denoting the fraction of longitudinally-polarized W bosons, and $F_{L,R}$, denoting the fraction of left/right-handed transversely-polarized W bosons. These helicity fractions have been measured at the Tevatron and LHC [58, 130–133] and in Table 10 we summarize the results used in our analysis. The experimental error is obtained by combining in quadrature the statistical and systematic errors reported by the experimental collaborations, and in the χ^2 function we consider correlations between F_0 and $F_{L,R}$. In addition to the helicity fraction, the ATLAS collaboration has measured the phase, δ^-, between the amplitudes for the longitudinally- and transversely-polarized W bosons, recoiling against a left-handed b quark, in the decay of a single top [58, 134]. This phase is sensitive to the imaginary parts of the dimension-six operators.

The SM helicity fractions have been computed at N^{2}LO in QCD [135]. They are a function of the ratio $x = m_W/m_t$, and, for the top pole mass, $m_t = 173$ GeV, and $m_W = 80.4$ GeV, the SM helicity fractions are $F_0 = 0.687$, $F_L = 0.311$, and $F_R = 0.0017$. The theoretical uncertainty is very small, at the permil level, and is negligible compared to the experimental error. The phase δ^- vanishes at tree level in the SM, but receives non-vanishing contributions from electroweak loops in which the internal W boson and b quark go on-shell [25]. However, these contributions are negligible with respect to the current experimental uncertainty.

The corrections to the helicity fractions induced by the operators C_{Wt} and C_{Wb} have been computed at NLO in QCD in Ref. [24]. Also in this case, the contribution of C_{Wb} is suppressed by the bottom Yukawa coupling and gives bounds that are not competitive with those from flavor physics. The LO correction of C_{Wt} to F_0 and F_L is [24]

$$F_0 = \frac{1 - 4y_t^2 x^2 (v^2 c_{Wt}) + 4x^4 y_t^4 \left((v^2 c_{Wt})^2 + (v^2 \tilde{c}_{Wt})^2\right)}{(1+2x^2) - 12 y_t^2 x^2 (v^2 c_{Wt}) + 4x^2(2+x^2) y_t^4 \left((v^2 c_{Wt})^2 + (v^2 \tilde{c}_{Wt})^2\right)} \tag{33}$$

$$F_L = \frac{2x^2 \left(1 - 4y_t^2 (v^2 c_{Wt}) + 4 y_t^4 \left((v^2 c_{Wt})^2 + (v^2 \tilde{c}_{Wt})^2\right)\right)}{(1+2x^2) - 12 y_t^2 x^2 (v^2 c_{Wt}) + 4x^2(2+x^2) y_t^4 \left((v^2 c_{Wt})^2 + (v^2 \tilde{c}_{Wt})^2\right)}. \tag{34}$$

At tree level, the SM and C_{Wt} contributions to F_R vanish. They are not zero at one loop [24]. In our analysis, we used the NLO expressions of Ref. [24]. Similar to the single top cross section, c_{Wt} interferes with the SM and gives rise to a genuine dimension-six effect, while the imaginary part of C_{Wt} corrects the helicity fractions at $\mathcal{O}(1/\Lambda^4)$.

The phase δ_- is linear in $\tilde{c}_{Wt}$ and, at tree level, is given by [58, 134]

$$\delta_- = V_{tb}^2 \arg\left((x - g_R)(1 - x g_R)^*\right), \qquad \text{with} \quad g_R = 2\frac{m_W}{v} y_t (v^2 c_{Wt} + i\, v^2 \tilde{c}_{Wt}). \tag{35}$$

4.2 Indirect constraints

4.2.1 Higgs production and decay

The Higgs production cross section and branching ratios are sensitive probes of couplings of the top quark to the Higgs boson, gluon, and photons. We already discussed the associated production of a Higgs boson and a $t\bar{t}$ pair, which provides a direct probe of the Higgs-top Yukawa coupling and the top chromo-dipole operator C_g. In the SM the dominant Higgs production mechanism is gluon fusion and proceeds via a top loop. Similarly, the Higgs boson decay into two photons, the Higgs discovery channel, gets a sizable contribution from a top loop. We can thus expect Higgs production and decay processes to be very sensitive to anomalous top couplings, in particular to the modification of the top Yukawa, C_Y, and to the top electromagnetic and color dipoles C_γ and C_g.

Through mixing onto $C_{\varphi W}$ and $C_{\varphi WB}$, the operators C_{Wt} and C_{Wb} also affect important Higgs production and decay mechanisms such as vector boson fusion (VBF), associated production of a Higgs boson and a W or Z boson (WH and ZH), and the WW^* and ZZ^* decay channels. However, in this case the contribution of the dimension-six operators is suppressed by one electroweak loop with respect to the SM contribution, which arises at tree level, such that the resulting bounds turn out to be negligible.

The observables we consider are the Higgs signal strengths, which are observed to be compatible with the SM [136, 137]. For a given Higgs production mechanism, $i \to h$, followed by the decay of the Higgs to the final state f, the signal strength is defined as

$$\mu_{i\to h\to f} = \frac{\sigma_{i\to h}}{\sigma_{i\to h}^{SM}} \frac{\Gamma_{h\to f}}{\Gamma_{h\to f}^{SM}} \Big/ \frac{\Gamma_{\rm tot}}{\Gamma_{\rm tot}^{SM}}, \tag{36}$$

where $\sigma_{i\to h}$ and $\sigma_{i\to h}^{SM}$ are, respectively, the production cross section in the channel i including the effects of dimension-six operators, and the production cross section in the SM. $\Gamma_{h\to f}$ and $\Gamma_{h\to f}^{SM}$ are the decay widths in the channel f, and $\Gamma_{\rm tot}$ and $\Gamma_{\rm tot}^{SM}$ the Higgs total width, with and without the inclusion of dimension-six operators. For $m_h = 125$ GeV, the SM Higgs total width is $\Gamma_{\rm tot}^{SM} = 4.07 \pm 0.16$ MeV [138].

The only production channel which is significantly affected by the operators we consider is gluon fusion. The gluon fusion cross section can be computed in terms of the effective operators $\mathcal{O}_{\varphi G}$ and $\mathcal{O}_{\varphi\tilde{G}}$ and is known at N^{2}LO in α_s [139–143]. The scalar and pseudoscalar top Yukawa couplings c_Y and $\tilde{c}_Y$ induce threshold corrections to $C_{\varphi G}$ and $C_{\varphi\tilde{G}}$ at the scale m_t, while the top chromo-dipole moments mix onto $\mathcal{O}_{\varphi G}$ and $\mathcal{O}_{\varphi\tilde{G}}$, with the anomalous dimension (10). As discussed in Ref. [51], the NLO and N^{2}LO corrections, and the theoretical uncertainties, mostly cancel in the ratio of the production cross section induced by $\mathcal{O}_{\varphi G}$ and $\mathcal{O}_{\varphi\tilde{G}}$ and the SM. We therefore use the tree-level expression, which, in the limit of $m_t \to \infty$, is given by

$$\frac{\sigma_{ggF}}{\sigma_{ggF}^{SM}} = \left(1 + v^2 c_Y(m_t^+) + 48\pi^2 v^2 C_{\varphi G}(m_t^+)\right)^2 + \left(48\pi^2 v^2 C_{\varphi\tilde{G}}(m_t^+) + \frac{3}{2} v^2 \tilde{c}_Y(m_t^+)\right)^2, \tag{37}$$

and neglect the small theoretical uncertainties. $C_{\varphi G}(m_t^+)$ is given in Table 3 and in Eq. (37) we explicitly show the threshold corrections induced by the anomalous scalar and pseudoscalar Yukawa couplings.

The decay channels most affected by the operators under consideration are $h \to gg$ and $h \to \gamma\gamma$. The gluonic decay of the Higgs is not directly observed at the LHC because of the large QCD background. However, it affects the signal strength by modifying the Higgs total width. In the infinite top mass limit, the Higgs decay width into gluons is [144],

$$\Gamma_{h\to gg} = \frac{\alpha_s^2 m_h^3}{72 v^2 \pi^3}\left(\left(1 + v^2 c_Y + 48\pi^2 v^2 C_{\varphi G}\right)^2 + \left(48\pi^2 v^2 C_{\varphi \tilde{G}} + \frac{3}{2} v^2 \tilde{c}_Y\right)^2\right), \tag{38}$$

where the couplings are evaluated at m_t^+.

The Higgs decay into photons in the infinite top mass limit becomes [144]

$$\frac{\Gamma_{h\to\gamma\gamma}}{\Gamma^{SM}_{h\to\gamma\gamma}} = \frac{\left(N_c Q_t^2 (1 + v^2 c_Y) + 24\pi^2 (v^2 C_{\varphi\gamma}) - \frac{21}{4} A(\tau_W)\right)^2 + \left(\frac{3}{2} N_c Q_t^2\, v^2 \tilde{c}_Y + 24\pi^2 (v^2 C_{\varphi\tilde{\gamma}})\right)^2}{\left(N_c Q_t^2 - \frac{21}{4} A(\tau_W)\right)^2}, \tag{39}$$

where the couplings are evaluated at m_t^+, $\tau_W = 4m_W^2/m_h^2$, and the loop function $A(\tau)$ is given in Eq. (25). The $\gamma\gamma$ channel gives negligible corrections to the total width. NLO QCD corrections to the SM decay widths $\Gamma^{SM}_{h\to\gamma\gamma}$ and $\Gamma^{SM}_{h\to gg}$ are known [144], and we included them in our analysis.

The signal strengths as measured by the ATLAS and CMS collaborations [136, 137] are given in Table 11. In our fits, we symmetrized the uncertainties in Table 11, and treated them as statistical errors.

5 Electroweak precision tests

The corrections from BSM physics to the self energies of the SM gauge bosons can be described by three parameters (up to terms linear q^2) [88–90],

$$\begin{aligned}
\frac{\alpha_w}{4 s_W^2 c_W^2} S &= \Pi'_{ZZ}(0) - \frac{c_W^2 - s_W^2}{c_W s_W}\Pi'_{\gamma Z}(0) - \Pi'_{\gamma\gamma}(0), \\
\alpha_w T &= \frac{\Pi_{WW}(0)}{m_W^2} - \frac{\Pi_{ZZ}(0)}{m_Z^2}, \\
\frac{\alpha_w}{4 s_W^2} U &= \Pi'_{WW}(0) - c_W^2 \Pi'_{ZZ}(0) - 2 s_W c_W \Pi'_{\gamma Z}(0) - s_W^2 \Pi'_{\gamma\gamma}(0),
\end{aligned} \tag{40}$$

where Π_{XY} denotes the self energy of the vector bosons X and Y, while the primes indicate differentiation with respect to q^2. Two of these parameters, S and T, are generated by dimension-six operators, namely $O_{\varphi WB}$ and $O_{HD} = \left|\varphi^\dagger D_\mu \varphi\right|^2$ [57, 90, 145],

$$S = 16\pi v^2 C_{\varphi WB}(m_t), \qquad T = -\frac{2\pi}{e^2} v^2 C_{HD}(m_t). \tag{41}$$

In contrast, the U parameter receives its first contribution at the dimension-eight level. As a result, when considering leading-log effects, the top-Higgs couplings only generate the S parameter, and do not contribute to C_{HD} or the dimension-eight operator responsible for U. The

ATLAS	gg	VBF	WH	ZH	$t\bar{t}h$
$\gamma\gamma$	1.3 ± 0.4	0.8 ± 0.7	1.0 ± 1.6	$0.1^{+3.7}_{-0.1}$	$1.3^{+2.6}_{-1.7}$
ZZ^*	1.7 ± 0.5	$\left(0.3^{+1.6}_{-0.9}\right)^\dagger$	–	–	–
WW^*	1.0 ± 0.3	1.3 ± 0.5	$3.0 \pm 1.6^*$	–	2.1 ± 1.4
$\tau\tau$	2.0 ± 1.5	$1.2 \pm 0.6^\dagger$	–	–	–
$b\bar{b}$	–	–	1.1 ± 0.6	0.05 ± 0.5	1.5 ± 1.1
CMS	gg	VBF	WH	ZH	$t\bar{t}h$
$\gamma\gamma$	1.1 ± 0.4	$1.2 \pm 0.6^\dagger$	–	–	2.7 ± 2.6
ZZ^*	0.8 ± 0.5	$1.7 \pm 2.2^\dagger$	–	–	–
WW^*	0.7 ± 0.2	0.6 ± 0.4	$0.4 \pm 2.0^*$	–	4.0 ± 1.8
$\tau\tau$	0.3 ± 0.9	$0.9 \pm 0.4^\dagger$	–	–	–
$b\bar{b}$	–	–	$0.8 \pm 0.4^*$	–	0.7 ± 1.9

Table 11: Higgs signal strength in various production and decay channels, as measured by the ATLAS and CMS collaborations [136, 137]. † denotes entries for which the signal strengths is given in the combined bosonic production modes (VBF + WH + ZH), $*$ denotes entries for which the combined WH + ZH signal strength is given.

contributions to S arise through the RG mixing with $O_{\varphi WB}$ described in section 3.1, which coincides with the divergent parts of the loop contributions discussed in [128, 146].

To derive the constraints resulting from the S parameter, we expres $C_{\varphi WB}$ in terms of the Higgs-top couplings (Table 3) and employ the result of a fit to experimental data, $S = -0.03 \pm 0.10$ [80] [9] [10].

6 Flavor physics

Flavor physics offers a large number of processes that can, in principle, receive contributions from the anomalous top interactions. However, we find that most of these observables only give rise to fairly weak constraints. We briefly discuss here flavor observables that are not very sensitive to these couplings, after which we turn to the $b \to s\gamma$ transitions which do lead to significant limits.

Starting in the B meson sector, the coupling c_{Wt} induces flavor-changing four-quark operators at one loop which can contribute to $\bar{B}_{d,s} - B_{d,s}$ mixing [147]. Comparing the resulting limits [147] to those coming from the rare B decays discussed below, we find that the B mixing constraints are weaker and do not affect our bounds significantly. We therefore neglect the $\bar{B}_{d,s} - B_{d,s}$ mixing observables in what follows.

In the kaon sector, there are potential constraints from similar observables as in the B-meson sector, although the uncertainties from long-distance effects are generally larger. Here, c_{Wt} induces a flavor-changing four-quark operator, analogous to the B-mixing operator, which contributes to CP violation in kaon mixing, ϵ_K. In addition, the top-Higgs couplings induce flavor-changing dipole operators. A gluonic dipole ($s \to dg$) is mainly generated by C_g and affects direct CP violation, ϵ', while $C_{\gamma,Wt}$ contribute to the photonic dipole operator ($s \to d\gamma$) which induces rare kaon decays such as $K_L \to \pi^+\pi^-\gamma$ [148]. We employ the expressions in Refs. [149], [150], and [148], to estimate the constraints from ϵ_K, ϵ', and rare decays, respectively. We find an $\mathcal{O}(1)$ constraint on $v^2 c_{Wt}$ in the case of ϵ_K, while the remaining observables give rise to weaker bounds. Thus, none of the above flavor observables leads to competitive constraints, and we focus on the limits coming from $b \to s\gamma$ transitions to be discussed below.

6.1 Rare B decays

To study the effects of the top-Higgs interactions on the $b \to s\gamma$ observables, namely the branching ratio and CP asymmetry, we closely follow the procedure outlined in Refs. [151, 152]. The branching ratio and CP asymmetry are mainly affected by the $C_{\gamma,g}^{(bs)}$ interactions induced by the top-Higgs operators. These couplings are related to the couplings $C_{7,8}$ that are more commonly

[9] This constraint results from a fit in which T and U are allowed to vary. Since we do not consider contributions to these parameters, we could take $T = U = 0$ to be a prediction of our scenario and force U and T to zero in the fit. This would lead to a more stringent constraint on S, with the SM point, $S = 0$, excluded at 90%. We therefore prefer to allow T and U to vary and employ the more conservative constraint $S = -0.03 \pm 0.10$.

[10] It should be noted that the extraction of S could be complicated in case there are additional interactions that significantly modify the fermion-Z vertex [74, 75]. Such deviations from the SM could be induced by operators of the form $(\bar{f}_{L,R}\gamma^\mu f_{L,R})(i\varphi^\dagger(\overleftarrow{D}_\mu - \overrightarrow{D}_\mu)\varphi)$, however, since these interactions only receive mixing contributions from the top-Higgs interactions at the three-loop level, we neglect these effects here.

used in the literature [44, 151–155], by the relations

$$C_\gamma^{(bs)} = \frac{V_{tb}V_{ts}^*}{4\pi^2 Q_b}\frac{C_7}{v^2}, \qquad C_g^{(bs)} = -\frac{V_{tb}V_{ts}^*}{4\pi^2}\frac{C_8}{v^2}\ . \tag{42}$$

The dimension-six contributions to these operators can be read off from Table 4.

6.1.1 BR $(B \to s\gamma)$

We describe the branching ratio by the expression derived in Refs. [154,156], rescaled to the SM prediction of [153, 157, 158],

$$\begin{aligned}\mathrm{BR}\,(B\to s\gamma) = 10^{-4}\frac{3.36}{2.98}\Big[&2.98 + 4.743|C_7^{\rm NP}|^2 + 0.789|C_8^{\rm NP}|^2 \\ &+\mathrm{Re}\left((-7.184+0.612i)C_7^{\rm NP} + (-2.225-0.557i)C_8^{\rm NP} + (2.454-0.884i)C_7^{\rm NP}C_8^{\rm NP*}\right)\Big],\end{aligned} \tag{43}$$

where $C_{7,8}^{\rm NP}$ stand for the non-standard contributions to $C_{7,8}$, which are to be evaluated at the top scale, $\mu = 160\,\mathrm{GeV}$. This expression should be compared with the current experimental world average [80],

$$\mathrm{BR}\,(B\to s\gamma) = (3.43 \pm 0.21 \pm 0.07)\times 10^{-4}. \tag{44}$$

In order to derive constraints we follow Refs. [151, 152] and use the relative uncertainty on the SM prediction as our theoretical error, $\sigma = \frac{0.23}{3.36}\mathrm{BR}(b\to s\gamma)$. This theoretical uncertainty is then added in quadrature to the experimental one.

6.1.2 $A_{CP}(B \to s\gamma)$

For the CP asymmetry we follow Refs. [44, 151, 152] and employ the expression derived in Ref. [155],

$$\begin{aligned}\frac{A_{CP}(B\to s\gamma)}{\pi} &\equiv \frac{1}{\pi}\frac{\Gamma(\bar B\to X_s\gamma)-\Gamma(B\to X_{\bar s}\gamma)}{\Gamma(\bar B\to X_s\gamma)+\Gamma(B\to X_{\bar s}\gamma)} \\ &\approx \left[\left(\frac{40}{81}-\frac{40}{9}\frac{\Lambda_c}{m_b}\right)\frac{\alpha_s}{\pi}+\frac{\Lambda_{17}^c}{m_b}\right]\mathrm{Im}\,\frac{C_2}{C_7} - \left(\frac{4\alpha_s}{9\pi}+4\pi\alpha_s\frac{\Lambda_{78}}{3m_b}\right)\mathrm{Im}\,\frac{C_8}{C_7} \\ &\quad -\left(\frac{\Lambda_{17}^u-\Lambda_{17}^c}{m_b}+\frac{40}{9}\frac{\Lambda_c}{m_b}\frac{\alpha_s}{\pi}\right)\mathrm{Im}\left(\frac{V_{ub}V_{us}^*}{V_{tb}V_{ts}^*}\frac{C_2}{C_7}\right),\end{aligned} \tag{45}$$

where C_2 is a four-quark operator, $\sim (\bar d_L\gamma^\mu b_L)(\bar s_L\gamma_\mu d_L)$ [159], which, along with $C_{7,8}$, should to be evaluated at the factorization scale $\mu_b \simeq 2$ GeV. We employ the following SM values for these coefficients at $\mu_b = 2\,\mathrm{GeV}$ [155],

$$C_2^{\rm SM} = 1.204, \qquad C_7^{\rm SM} = -0.381, \qquad C_8^{\rm SM} = -0.175. \tag{46}$$

The contributions from the top-Higgs couplings at $\mu = m_t$ and $\mu = 2$ GeV can again be read from Table 4. In addition, the CP asymmetry depends on the scale, $\Lambda_c \simeq 0.38\,\mathrm{GeV}$, and on three hadronic parameters that are estimated to lie in the following ranges [155],

$$\Lambda_{17}^u \in [-0.33,\,0.525]\,\mathrm{GeV}, \qquad \Lambda_{17}^c \in [-0.009,\,0.011]\,\mathrm{GeV}, \qquad \Lambda_{78} \in [-0.017,\,0.19]\,\mathrm{GeV}. \tag{47}$$

	d_e	d_n	$d_{\rm Hg}$	$d_{p,D}$	$d_{\rm Xe}$	$d_{\rm Ra}$
current limit	$8.7 \cdot 10^{-29}$	$3.0 \cdot 10^{-26}$	$6.2 \cdot 10^{-30}$	x	$5.5 \cdot 10^{-27}$,	$4.2 \cdot 10^{-22}$
expected limit	$5.0 \cdot 10^{-30}$	$1.0 \cdot 10^{-28}$	$6.2 \cdot 10^{-30}$	$1.0 \cdot 10^{-29}$	$5.0 \cdot 10^{-29}$	$1.0 \cdot 10^{-27}$

Table 12: Current limits on the electron [162], neutron [163,164], and mercury [165,166] EDMs in units of e cm (90% confidence level). We also show an indication of their prospective limits [167,168] as well as those of the proton, deuteron, xenon [169], and radium [170] EDMs, which could provide interesting constraints in the future.

We deal with these rather large uncertainties by using the R-fit procedure [160]; we vary the Λ parameters in their allowed ranges, selecting the values which produce the smallest χ^2. The final ingredient we require is the current experimental value of the CP asymmetry given by [161]

$$A_{CP}(B \to s\gamma) = 0.015 \pm 0.02. \tag{48}$$

7 Electric dipole moments

Permanent EDMs of leptons, nucleons, nuclei, atoms, and molecules probe flavor-diagonal CP violation with essentially no SM background. CP violation from the CKM mechanism predicts EDMs that are orders of magnitude below current experimental sensitivities. The only SM background then arises from the QCD vacuum angle, the so-called theta term, which, in principle, induces large EDMs of hadrons and nuclei. The absence of an experimental signal for the neutron and ^{199}Hg EDMs leads to the strong constraint $\theta < 10^{-10}$ [171]. This smallness begs for an explanation that can be provided by the Peccei-Quinn mechanism [172], which dynamically relaxes the vacuum angle to zero at the cost of a, so far, unmeasured axion. In this work, we assume the Peccei-Quinn mechanism to be at work such that the bare theta term is removed from our EFT. However, in the presence of dimension-six sources of CP violation, the Peccei-Quinn mechanism does not completely remove the theta term. Instead, the vacuum angle is relaxed to a finite value proportional to the coefficients of the dimension-six CPV operators. The contribution from the induced vacuum angle is taken into account in our analysis by the value of the hadronic matrix elements [173]. Recent developments in lattice QCD [174–178] and chiral effective field theory [179, 180] have improved the description of hadronic and nuclear EDMs. If future experiments detect nonzero EDMs, their precise pattern could potentially disentangle a nonzero theta term from BSM sources of CP violation [85]. For now, however, we apply the Peccei-Quinn mechanism to essentially remove the theta term from our analysis.

At present, the most stringent constraints come from measurements of the neutron, ^{199}Hg atom, and ThO molecule EDMs. Here we give a brief overview of our analysis of these EDMs and refer to Ref. [51] for more details.

We begin with ThO measurement [162], which, for the set of dimension-six operators under discussion, can be interpreted as a measurement of the electron EDM[11]

$$d_e = e\, Q_e m_e \tilde{c}_\gamma^{(e)}(\Lambda_\chi) \quad \leq \quad 8.7 \cdot 10^{-29}\, e\,\text{cm} \quad (90\%\,\text{C.L.}) \ . \tag{49}$$

[11] Apart from the electron EDM, the ThO EDM also receives contributions from semi-leptonic four-fermion interactions, which can be generated by the top-Higgs couplings at loop-level. However, these induced semi-leptonic interactions are always negligible due to suppression by small Yukawa couplings and/or CKM elements.

This rather clean theoretical interpretation in terms of the electron EDM involves an estimated $\mathcal{O}(15\%)$ uncertainty [181, 182]. As this error estimate only affects the bound by an overall factor (it does not allow for cancellations) and it is far below the uncertainties related to the hadronic/nuclear EDMs, we neglect it here.

The neutron and proton EDMs are plagued by much larger hadronic uncertainties. They can be expressed in terms of the operators of Eq. (5e) via the relations

$$\begin{aligned} d_n &= -(0.22 \pm 0.03)\, e\, Q_u m_u \tilde{c}_\gamma^{(u)} + (0.74 \pm 0.07)\, e\, Q_d m_d \tilde{c}_\gamma^{(d)} + (0.0077 \pm 0.01)\, e\, Q_s m_s \tilde{c}_\gamma^{(s)} \\ &\quad -(0.55 \pm 0.28)\, e\, m_u \tilde{c}_g^{(u)} - (1.1 \pm 0.55)\, e\, m_d \tilde{c}_g^{(d)} \pm (50 \pm 40) e\, g_s C_{\tilde{G}}, \\ d_p &= (0.74 \pm 0.07)\, e\, Q_u m_u \tilde{c}_\gamma^{(u)} - (0.22 \pm 0.03)\, e\, Q_d m_d \tilde{c}_\gamma^{(d)} + (0.0077 \pm 0.01)\, e\, Q_s m_s \tilde{c}_\gamma^{(s)} \\ &\quad +(1.30 \pm 0.65)\, e\, m_u \tilde{c}_g^{(u)} + (0.60 \pm 0.30)\, e\, m_d \tilde{c}_g^{(d)} \mp (50 \pm 40) e\, g_s C_{\tilde{G}}, \end{aligned} \tag{50}$$

where all coefficients should be evaluated at $\mu = \Lambda_\chi$. Because of recent lattice calculations [175, 183], the contributions from the up- and down-quark EDMs in this expression are known to $\mathcal{O}(15\%)$, while the strange contribution is still highly uncertain. The up- and down-quark CEDM contributions have an estimated 50% uncertainty based on QCD sum-rule calculations [173, 184–186], while the Weinberg operator appears with the largest uncertainty, $\mathcal{O}(100\%)$, based on a combination of QCD sum-rules [187] and naive dimensional analysis estimates [77]. The magnitude of the strange-quark CEDM contribution is currently unresolved and is often assumed to vanish in the Peccei-Quinn scenario. We do so here as well, but point out that this assumption might be unwarranted [188].

Finally, the ^{199}Hg EDM receives contributions from the nucleon EDMs as well as from the CP-odd isoscalar and isovector pion-nucleon couplings[12], $\bar{g}_0$ and $\bar{g}_1$ (here we use the conventions of Ref. [51]). The induced nucleon EDMs are given above, while the pion-nucleon couplings are generated by the quark CEDMs [189],

$$\bar{g}_0 = (5 \pm 10)(m_u \tilde{c}_g^{(u)} + m_d \tilde{c}_g^{(d)})\,\mathrm{fm}^{-1} \ , \qquad \bar{g}_1 = (20^{+40}_{-10})(m_u \tilde{c}_g^{(u)} - m_d \tilde{c}_g^{(d)})\ \mathrm{fm}^{-1} \ . \tag{51}$$

Combining the contributions of the nucleon EDMs [190] with those of the pion-nucleon couplings [191–194], then gives the following expression for the ^{199}Hg EDM,

$$d_{\mathrm{Hg}} = -(2.8 \pm 0.6) \cdot 10^{-4} \left[(1.9 \pm 0.1) d_n + (0.20 \pm 0.06) d_p + \left(0.13^{+0.5}_{-0.07}\, \bar{g}_0 + 0.25^{+0.89}_{-0.63}\, \bar{g}_1 \right) e\,\mathrm{fm} \right], \tag{52}$$

where the small number in front of the main brackets is the Schiff screening factor. The large nuclear uncertainties appearing in the dependencies on $\bar{g}_{0,1}$ dilute the constraining power of d_{Hg}.

We summarize the current and prospective limits in Table 12. The table also shows the limits on systems which are not yet competitive, but could provide interesting constraints in the future. EDM experiments on ^{225}Ra and ^{129}Xe atoms have already provided limits [169,170] and are quickly improving. We use the following expressions for these EDMs [194]

$$d_{\mathrm{Xe}} = (0.33 \pm 0.05) \cdot 10^{-4} \left(-0.10^{+0.037}_{-0.53}\, \bar{g}_0 - 0.076^{+0.038}_{-0.55}\, \bar{g}_1 \right) e\,\mathrm{fm} \ , \tag{53}$$

$$d_{\mathrm{Ra}} = -(7.7 \pm 0.8) \cdot 10^{-4} \left(-19^{+6.4}_{-57}\, \bar{g}_0 + 76^{+227}_{-25}\, \bar{g}_1 \right) e\,\mathrm{fm} \, . \tag{54}$$

[12] A potential third contribution from a CP-odd isotensor pion-nucleon interaction is negligible for all operators in Eq. (5e) [179].

We point out that these expressions do not contain the dependencies on the single-nucleon EDMs as these have, as far as we know, not been calculated. The associated nuclear uncertainties are still significant but smaller than for $d_{\rm Hg}$. $d_{\rm Ra}$ has the additional benefit of a smaller screening factor and a large dependence on $\bar{g}_{0,1}$ due to the octopole deformation of the nucleus (see Ref. [194] and references therein).

Plans exist to measure the EDMs of charged nuclei in electromagnetic storage rings [195]. Here we consider the impact of a deuteron EDM measurement. Light nuclei have the advantage that the theoretical calculations can be performed accurately within a controlled power counting scheme [196, 197]. The deuteron EDM can be expressed as

$$d_D \;=\; (0.94 \pm 0.01)(d_n + d_p) + (0.18 \pm 0.02)\bar{g}_1\, e\,\text{fm}\ , \tag{55}$$

which, as this is a measurement of a nuclear EDM, has no Schiff screening factor. EDMs of other light nuclei, such as ^{3}He , ^{6}Li , and ^{13}C have been investigated along similar lines [196–201] but are not considered here.

7.1 Lepton anomalous magnetic moments

The same mechanisms that generate the electron dipole moment $\tilde{c}_\gamma^{(e)}$ also induce the magnetic moments of charged leptons. As the magnetic moments of the electron [202] and muon [203] are measured to very high accuracy and have precise SM predictions, we briefly discuss whether they lead to significant constraints on the top-Higgs couplings. The magnetic moment is defined as

$$\vec{M}_l = \frac{e}{2m_l} g_l \vec{S}, \tag{56}$$

where $l = (e,\, \mu,\, \tau)$, $\vec{S}$ is the spin of the charged lepton, and $g_l = 2$ at tree level in the SM. Loop effects in the SM lead to corrections to g_l, thereby inducing anomalous magnetic moments,

$$a_l = \frac{g_l - 2}{2}. \tag{57}$$

Due to the small uncertainties in the measurement of a_e [202], it can be used to obtain the most precise value of the electromagnetic fine-structure constant [204]. To instead compare the measurement to the SM value of a_e, the fine-structure constant has to be extracted from an independent experiment. Currently, the most precise determination (apart from a_e) comes from a measurement of the ratio of Planck's constant and the mass of the ^{87}Rb atom [205]. Employing the obtained fine structure constant and comparing the SM predictions for $a_{e,\,\mu}$ with the experimental results gives [80],

$$\begin{aligned} \Delta a_e &= a_e^{\rm exp} - a_e^{\rm SM} = -1.05(0.82)\cdot 10^{-12}\,, \\ \Delta a_\mu &= a_\mu^{\rm exp} - a_\mu^{\rm SM} = 2.88(0.63)(0.49)\cdot 10^{-9}, \end{aligned} \tag{58}$$

where a_μ is in some tension with the SM prediction while a_e is consistent with the SM.

The real parts of the top couplings in Eq. (2) induce corrections to the lepton magnetic moments in the same way as the imaginary parts induce the electron EDM. For c_Y this occurs through Barr-Zee diagrams, Eq. (26), while for $c_{\gamma,\,g,\,Wt,\,Wb}$ the main contributions arise through

the two-step mechanism explained in Section 3.3. Extending Eq. (5e) to include the fermion magnetic dipole operators, we can parametrize the corrections to a_l as

$$\Delta a_l = -2\frac{m_l^2}{v^2} Q_l \left(v^2 c_\gamma^{(l)}(\Lambda_\chi) \right). \tag{59}$$

Since the running of the real and imaginary part of the operators C_α in Eq. (2) onto the lepton magnetic and electric dipole operators is identical, the values of $c_\gamma^{(l)}(\Lambda_\chi)$ as a function of the top couplings at the scale $\Lambda = 1$ TeV can be read from the first line of Table 5, giving

$$\begin{aligned} \Delta a_e &= \left(3.3\,(v^2 c_\gamma) + 0.12\,(v^2 c_g) - 3.8\,(v^2 c_{Wt}) + 0.35\,(v^2 c_Y)\right) \cdot 10^{-15}\,, \\ \Delta a_\mu &= \left(13.8\,(v^2 c_\gamma) + 0.51\,(v^2 c_g) - 16.0\,(v^2 c_{Wt}) + 1.5\,(v^2 c_Y)\right) \cdot 10^{-11}, \end{aligned} \tag{60}$$

where the contribution of c_{Wb} is negligible.

Comparing with Eq. (58) we see that the uncertainty on Δa_e is a factor $\mathcal{O}(10^3)$ smaller than on Δa_μ, while the latter is more sensitive to the top-Higgs couplings by a factor $m_\mu^2/m_e^2 \sim 4 \cdot 10^4$. Despite this sensitivity, large values of the couplings, $v^2\, c_\alpha \sim \mathcal{O}(10) - \mathcal{O}(100)$, are needed to explain the observed tension with the SM. Furthermore, the determination of Δa_e leads to $\mathcal{O}(100)$ constraints on $v^2\, c_\alpha$. As we discuss in Section 9, such large values are already excluded by other direct and indirect observables. This implies that the $g_\mu - 2$ anomaly cannot be due to the dimension-six operators we investigate, and Δa_e does not give competitive constraints. We therefore do not include the electron and muon anomalous magnetic moments in our analysis.

8 Analysis strategy

8.1 The χ^2 functions

To set constraints on the top-Higgs couplings using a given observable we construct a χ^2 in the usual way,

$$\chi_i^2 = \left(\frac{\mathcal{O}_i^{\rm th} - \mathcal{O}_i^{\rm exp}}{\sigma_i} \right)^2. \tag{61}$$

Here $\mathcal{O}_i^{\rm exp}$ stands for the experimentally measured value of the observable i, $\mathcal{O}_i^{\rm th}$ is its theoretical expression, and σ_i is the related experimental uncertainty.[13] As there is a large number of observables to consider, we combine them in a number of ways. For the collider observables, we differentiate between direct and indirect constraints,

$$\chi^2_{\rm direct} = \sum_{i=t,\, t\bar{t},\, t\bar{t}h,\, F_0,\, F_L,\, F_R,\, \delta_-} \chi_i^2, \qquad \chi^2_{\rm indirect} = \sum_{i,j} \chi^2_{i\to h(W,Z)\to j}, \tag{62}$$

where the indirect constraints include all the Higgs production and decay channels, mentioned in Section 4. The direct constraints include t, $t\bar{t}$, and $t\bar{t}h$ production, as well as the W helicity fractions, while the constraint from the electroweak precision tests are simply captured by χ^2_S.

[13] There is one exception to this in the case of BR($b \to s\gamma$). As described in section 6.1.1, in this case we treat the theory error as statistical and add it to the experimental one in quadrature, i.e. $\sigma^2 = (\sigma^{\rm th})^2 + (\sigma^{\rm exp})^2$.

For the rare B decays we combine the constraints from both observables into a single constraint,

$$\chi^2_{b\to s\gamma} = \chi^2_{\rm BR} + \chi^2_{A_{CP}}. \tag{63}$$

Finally the EDM constraints are combined into a single χ-squared as follows,

$$\chi^2_{\rm EDMs} = \sum_{i=d_n,\, d_{\rm Hg},\, d_{\rm ThO},\, d_p,\, d_D,\, d_{\rm Ra},\, d_{\rm Xe}} \chi^2_i, \tag{64}$$

where the final four observables are typically only relevant when considering future constraints. The combined χ^2, taking into account all observables, is then given by,

$$\chi^2_{\rm Total} = \chi^2_{\rm direct} + \chi^2_{\rm indirect} + \chi^2_S + \chi^2_{b\to s\gamma} + \chi^2_{\rm EDMs}. \tag{65}$$

8.2 Theoretical uncertainties

Through $\mathcal{O}_i^{\rm th}$ the above χ^2 functions depend on both the top-Higgs couplings (at the scale Λ), as well as parameters which have theoretical uncertainties. In the case of high-energy probes these 'parameters' are the theory prediction for the SM and BSM contributions to cross sections and signal strengths, while for the $b \to s\gamma$ observables and EDMs the hadronic and nuclear matrix elements play the role of these parameters. We deal with these theoretical uncertainties in two different ways:

- **Central:** Here we neglect theoretical uncertainties in the hadronic and nuclear matrix elements entering d_n, $d_{\rm Hg}$ and A_{CP}. Instead, for collider observables, where the uncertainties are under better control and generally smaller, we apply the R-fit procedure explained below.

- **R-fit:** Here we vary all theoretical uncertainties, appearing in d_n, $d_{\rm Hg}$, A_{CP}, and collider observables, within the allowed ranges assuming a flat distribution, and minimize the total χ^2. This method corresponds to the Range-fit (R-fit) procedure defined in Ref. [160]. It always gives the weakest (= most conservative) constraint as it allows for cancellations between different contributions.

9 Discussion

9.1 Single coupling analysis

We first focus on the case in which a single operator dominates at the high scale. In Figs. 3 and 4 we show the 90% C.L. allowed region for the complex couplings C_γ, C_{Wt}, C_{Wb}, C_g and C_Y, obtained under the assumption that only one coupling is nonzero at a scale $\Lambda = 1$ TeV (the bounds on the dimensionless parameters do not significantly change if larger values of Λ are applied). For each coupling we show the combined allowed region (black), and the most constraining bounds coming from EDMs (red), flavor physics (green), electroweak precision observables (blue), and direct and indirect collider searches (orange). Theoretical uncertainties play a large role for the constraints arising from EDMs and flavor observables. The plots in Fig. 3 and 4 are obtained with the R-fit procedure described in Section 8 which particularly affects the constraints on the imaginary parts of the couplings [51].

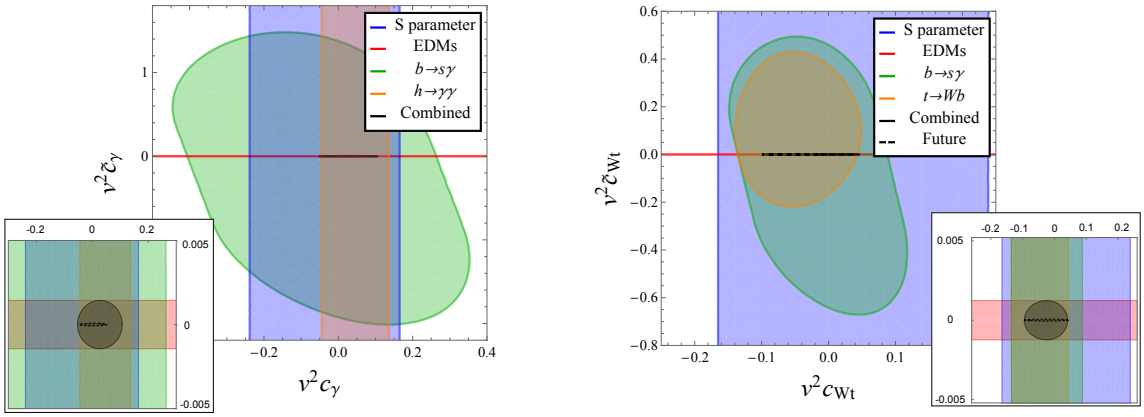

Figure 3: 90% C.L. allowed regions in the $v^2 c_\gamma - v^2\tilde{c}_\gamma$ (left panel) and $v^2 c_{Wt} - v^2\tilde{c}_{Wt}$ planes (right panel), with couplings evaluated at $\Lambda = 1$ TeV. In both cases, the inset zooms into the current combined allowed region and shows projected future sensitivities.

The dashed black contour denotes future sensitivities, considering improvements in EDM experiments [167], super-B factory measurements [206, 207], and collider searches [208, 209]. For the electron and neutron EDM we use the expected limits in Table 12, which project an improvement on the electron and neutron EDMs by a factor of 10 and 100, respectively. We assume the bound on $d_{\rm Hg}$ to stay at the current level. Future super-B factory experiments can reduce the statistical error on the $b \to s\gamma$ branching ratio to about 3%, and improve the error on A_{CP} by a factor of 5 [206, 207]. For the Higgs signal strengths, we use the projected uncertainties of Ref. [208,209] for the LHC Run 2, with $\sqrt{S} = 14$ TeV, and integrated luminosity of 300 fb^{-1}. We assume a central value of 1 (SM prediction) in every production and decay channel. The projected uncertainty on the gluon fusion channel with decay in $\gamma\gamma$ and ZZ^*, $\mu_{gg\to h\to\gamma\gamma}$ and $\mu_{gg\to h\to ZZ^*}$, is about 10%, while uncertainties in other relevant channels range from 20% on $\mu_{gg\to h\to WW}$ and $\mu_{VBF\to h\to\gamma\gamma}$, to 30%-40% on $\mu_{h\to b\bar{b}}$ and $\mu_{t\bar{t}h}$. For all observables, we do not assume improvement in the theoretical uncertainties, but stress that improvements on hadronic/nuclear matrix elements could have a large impact on EDM constraints [51].

In the single operator analysis, EDMs put extremely strong bounds on the imaginary parts of the coefficients C_α. This is true in particular for $\tilde{c}_\gamma$ and $\tilde{c}_{Wt}$. As shown in Fig. 3, the mixing of these operators into the electron EDM leads to constraints that are a factor of 10^3 stronger [52] than constraints from the A_{CP} asymmetry in $b \to s\gamma$ or from the phase δ^- measured in top decays. The current bound on the electron EDM limits c_γ to be $|v^2\tilde{c}_\gamma| < 1.4 \cdot 10^{-3}$. The real part of the coupling, c_γ, can be larger and is mainly constrained by the S parameter and by Higgs decay into photons. We find the allowed region for c_γ to be $-0.05 < v^2 c_\gamma < 0.11$ (90% C.L.). Projected experimental improvements on the electron EDM can improve the bounds on $\tilde{c}_\gamma$ by a factor of 10, while the LHC Run 2 has the possibility of improving the bound on the real part by a factor of 2. Additional direct information on the real part can be obtained by studying additional observables at LHC Run 2 in processes such as $\bar{t}t + \gamma$, $\bar{t}t + Z$ [32, 49].

The situation is similar for C_{Wt}. In the single operator analysis, the imaginary part of C_{Wt} is extremely well constrained by the electron EDM, $|v^2\tilde{c}_{Wt}| < 1.2 \cdot 10^{-3}$. Bounds from A_{CP} and δ^- are more than a hundred times weaker. In this case, the real part of the coupling receives competitive constraints from $b \to s\gamma$, the S parameter, single top production, and the W boson

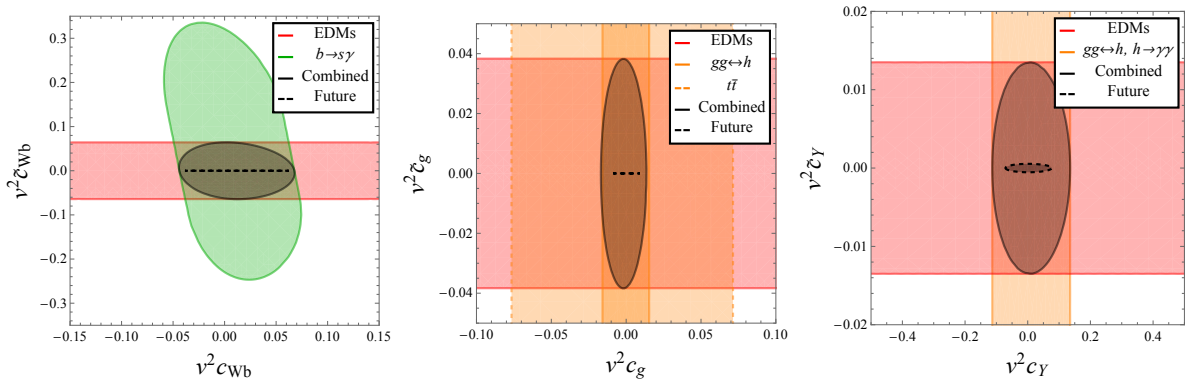

Figure 4: 90% C.L. allowed regions in the $v^2 c_{Wb} - v^2\tilde{c}_{Wb}$ (left panel) and $v^2 c_g - v^2\tilde{c}_g$ (center panel) and $v^2 c_Y - v^2\tilde{c}_Y$ (right panel) planes, with couplings evaluated at $\Lambda = 1$ TeV.

helicity fractions. The combined allowed region for c_{Wt} is $-0.10 < v^2 c_{Wt} < 0.04$ (90% C.L).

The left panel of Fig. 4 shows the allowed region for the coupling C_{Wb}. The EDM bound is dominated by the neutron EDM and is five time stronger than the limit extracted from A_{CP}, even with the conservative treatment of the theoretical errors that we are adopting. We find $|v^2\tilde{c}_{Wb}| < 0.06$. The real part, c_{Wb}, is mainly constrained by the $b \to s\gamma$ branching ratio yielding $-0.04 < v^2 c_{Wb} < 0.07$. Collider observables, like $Z \to b\bar{b}$ or single top production, and indirect observables like the S parameter, give much weaker bounds, $v^2 c_{Wb} \sim O(1) - \mathcal{O}(10)$. A neutron EDM bound at the level of 10^{-28} e cm, which should be in reach of the next generation of EDM experiments, would strengthen the constraint on $\tilde{c}_{Wb}$ by a factor of 100 even without improvements on the hadronic matrix elements. The impact of future super-B factory experiments appears to be more limited and only slightly affect the bound on c_{Wb}.

The center and right panels of Fig. 4 show, respectively, the allowed regions for C_g and C_Y. As shown in Table 5, $\tilde{c}_g$ contributes to both the neutron and the electron EDM. In the R-fit procedure, the neutron EDM is subject to cancellations between the contributions of the Weinberg operator and those of the light quark (C)EDMs. This severely weakens the neutron EDM constraint, such that the strongest bound comes from the electron EDM and we obtain $|v^2\tilde{c}_g| < 0.038$. This constraint can be significantly improved with a better understanding of the effect of the Weinberg operator on the neutron EDM [51]. The top chromo-magnetic dipole moment, c_g, strongly affects the gluon fusion Higgs production channel and the decay width $h \to gg$, resulting in a very strong bound $-0.017 < v^2 c_g < 0.014$. In the center panel of Fig. 4 we compare the bound on c_g from gluon fusion and the direct bound from the $t\bar{t}$ production cross section. Notwithstanding the sizable experimental uncertainties on the Higgs signal strengths, the indirect bound is already five time stronger than the direct bound from $t\bar{t}$. c_g also contributes to the associated production of a Higgs boson and a $t\bar{t}$ pair. At the moment, the bound from $t\bar{t}h$ is not competitive with gluon fusion or $t\bar{t}$. Data from the LHC Run 2 will improve the bound on c_g to the sub-percent level, while new neutron and electron EDM experiments are projected to improve the bound on $\tilde{c}_g$ by one to two orders of magnitude.

In the single operator scenario, the pseudo-scalar Yukawa, $\tilde{c}_Y$, receives its strongest bound from the electron EDM, $|v^2\tilde{c}_Y| < 0.013$. The real part of the anomalous Yukawa coupling, c_Y, affects the Higgs gluon fusion production cross section and the decays $h \to gg$ and $h \to \gamma\gamma$. c_Y can also be probed directly by studying the associated $t\bar{t}h$ production. With the current

Real	**R-fit**	Imaginary	**R-fit**	**Central**
$v^2\, c_\gamma$	$[-5.3, 11] \cdot 10^{-2}$	$v^2\, \tilde{c}_\gamma$	$[-1.4, 1.4] \cdot 10^{-3}$	$[-1.4, 1.4] \cdot 10^{-3}$
$v^2\, c_{Wt}$	$[-9.5, 4.2] \cdot 10^{-2}$	$v^2\, \tilde{c}_{Wt}$	$[-1.2, 1.2] \cdot 10^{-3}$	$[-1.2, 1.2] \cdot 10^{-3}$
$v^2\, c_{Wb}$	$[-4.4, 6.7] \cdot 10^{-2}$	$v^2\, \tilde{c}_{Wb}$	$[-6.4, 6.4] \cdot 10^{-2}$	$[-4.2, 4.4] \cdot 10^{-3}$
$v^2\, c_g$	$[-1.7, 1.4] \cdot 10^{-2}$	$v^2\, \tilde{c}_g$	$[-3.8, 3.8] \cdot 10^{-2}$	$[-2.9, 2.9] \cdot 10^{-4}$
$v^2\, c_Y$	$[-12, 14] \cdot 10^{-2}$	$v^2\, \tilde{c}_Y$	$[-1.3, 1.3] \cdot 10^{-2}$	$[-1.3, 1.3] \cdot 10^{-2}$

Table 13: Allowed region (90% C.L.) for the couplings C_α, with the assumption that one complex coupling is turned on at the scale $\Lambda = 1$ TeV. Constraints in the second and third columns are obtained by using the R-fit strategy of Sect. 8.2, while the constraints on the imaginary couplings in the fourth column are based on central matrix elements.

experimental data, the bound is dominated by the Higgs signal strengths and is at the 10% level, $-0.12 < v^2 c_Y < 0.14$. The bound from $t\bar{t}h$ is noticeably weaker (and has a preference for positive values of c_Y), $-0.1 < v^2 c_Y < 1.1$ and is not shown in Fig. 4.

9.1.1 Summary

The constraints shown in Figs. 3 and 4 are summarized in Table 13. EDM limits provide the most stringent constraints for all the imaginary parts of the top-Higgs couplings, which are therefore generally constrained to be smaller than the real parts by one order of magnitude or more. Exceptions are C_g and C_{Wb} where the imaginary parts can still be of the same order as the real parts. In part, these exceptions are due to the large hadronic uncertainties related to the Weinberg operator, which in the case of $\tilde{c}_g$ allows the contributions to the neutron EDM to cancel completely. Clearly, a better understanding of the relevant matrix element would lead to improvement of these constraints. To illustrate this, in the fifth column of Table 13 we also give the bounds that can be set on the imaginary couplings if we ignore the uncertainties in the matrix elements and simply use central values. This has a large impact on the couplings $\tilde{c}_{Wb}$ and $\tilde{c}_g$ illustrating the importance of improving the theoretical understanding of CPV operators in nucleons and nuclei.

The real parts of the couplings are constrained by a more diverse set of observables. Higgs production and decay processes provide the most stringent constraints on c_γ ($h \to \gamma\gamma$), c_g ($gg \to h$), and c_Y (both $gg \to h$ and $h \to \gamma\gamma$). The weak dipole operator c_{Wb} is constrained purely by its contribution to the $b \to s\gamma$ transition, while for c_{Wt} the W helicity fractions give rise to slightly stronger constraints. Finally, the S parameter provides competitive constraints in the case of c_γ and c_{Wt}. We find that the constraints are not significantly affected by theoretical uncertainties and find only small differences when using central matrix elements.

The constraints in Table 13 were derived truncating the expansion of observables at $\mathcal{O}(v^2/\Lambda^2)$, including only genuine dimension-six effects. We explicitly checked that dimension-eight effects in the collider cross sections and signal strengths, and in $b \to s\gamma$, do not significantly impact the bounds.

Finally, we notice that for c_γ, c_{Wt}, c_{Wb}, c_Y, $\tilde{c}_Y$, $\tilde{c}_g$ and the bounds on c_g from $t\bar{t}$ production, our results are compatible with the existing literature (for example, Refs. [12,30,31,33,35,44,46–48]).

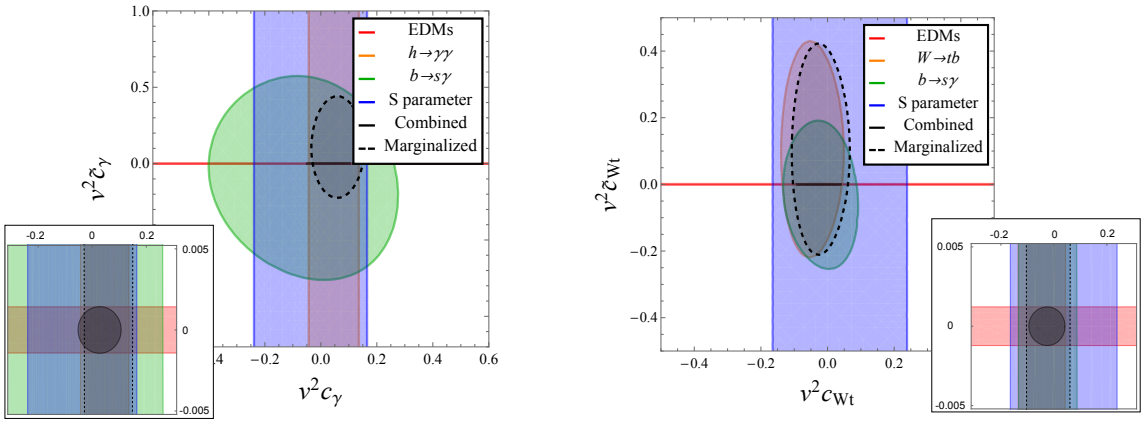

Figure 5: Same as Fig. 3, showing the 90% C.L. allowed regions in the $v^2c_\gamma - v^2\tilde{c}_\gamma$ (left panel) and $v^2c_{Wt} - v^2\tilde{c}_{Wt}$ planes (right panel), but now assuming central values for the relevant nuclear and hadronic matrix elements. Both the allowed regions in the single coupling case (solid lines) and marginalized case (dashed lines) are shown.

For $\tilde{c}_\gamma$, $\tilde{c}_{Wt}$, $\tilde{c}_{Wb}$, we find that EDMs provide stronger bounds than previously realized. For c_g, the strongest constraint comes from the contribution to Higgs production through gluon fusion.

9.2 Global fit

We now investigate the scenario in which new physics generates all the operators in Eq. (2) at the high scale $\Lambda = 1$ TeV, with arbitrary coefficients. This scenario allows us to quantify the effects of possible cancellations between contributions from various top couplings to direct and indirect observables, and to test the robustness of the strong EDM bounds discussed in Section 9.1.

The large theoretical uncertainties of the hadronic and nuclear matrix elements entering the mercury EDM cause the bound from $d_{\rm Hg}$ to effectively disappear in the R-fit approach, reducing the number of CP-odd observables to four (electron and neutron EDMs, A_{CP} in $b \to s\gamma$, and the phase δ^- in top decays). As we investigate five anomalous couplings, this gives rise to free directions for the imaginary parts leading to unbound $\tilde{c}_\alpha$ for all α apart from $\tilde{c}_{Wt}$ which remains constrained by the W helicity fractions discussed in Section 4.1.4. This situation is certainly unrealistic and requires an unmotivated cancellation between various couplings and matrix elements. Furthermore, the free directions can be removed by including less sensitive observables which we have neglected so far, or by including dimension-eight effects such as contributions of $\tilde{c}_\alpha$ to CPC total cross sections and decay rates, which become relevant for $v^2\tilde{c}_\alpha \sim O(1)$ (of course, this does not protect us from further cancellations against possible dimension-eight BSM operators). The latter possibility is, however, at the limit of validity of our assumption that the leading effects of BSM physics are captured by non-renormalizable operators of lowest canonical dimension. Finally, future EDM measurements on systems such as the proton, deuteron, or radium can also remove unconstrained directions [51].

In the rest of this Section we study one case in which the C_α can be bound, that is if we neglect theoretical uncertainties in the hadronic and nuclear matrix elements entering d_n, $d_{\rm Hg}$ and A_{CP}. Although this might seem rather wishful at the moment, relatively modest improvements from

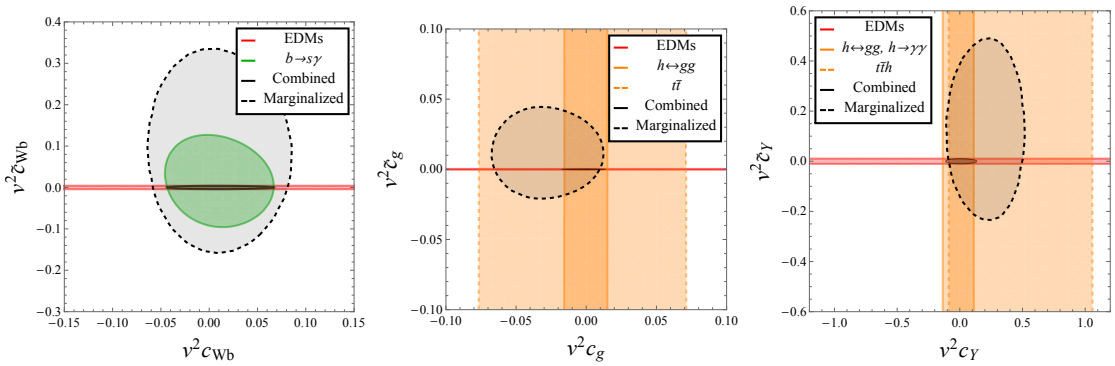

Figure 6: Same as Fig. 4, showing the 90% C.L. allowed regions in the $v^2 c_{Wb} - v^2 \tilde{c}_{Wb}$ (left panel) and $v^2 c_g - v^2 \tilde{c}_g$ (center panel) and $v^2 c_Y - v^2 \tilde{c}_Y$ (right panel) planes, but now assuming central values for the relevant nuclear and hadronic matrix elements. Both the allowed regions in the single coupling case (solid lines) and marginalized case (dashed lines) are shown.

Real	**Individual**	**Marginalized**	Imaginary	**Individual**	**Marginalized**
$v^2\, c_\gamma$	$[-5.3, 11] \cdot 10^{-2}$	$[-3.4, 15] \cdot 10^{-2}$	$v^2\, \tilde{c}_\gamma$	$[-1.4, 1.4] \cdot 10^{-3}$	$[-22, 44] \cdot 10^{-2}$
$v^2\, c_{Wt}$	$[-9.5, 4.2] \cdot 10^{-2}$	$[-11, 6.8] \cdot 10^{-2}$	$v^2\, \tilde{c}_{Wt}$	$[-1.2, 1.2] \cdot 10^{-3}$	$[-21, 42] \cdot 10^{-2}$
$v^2\, c_{Wb}$	$[-4.4, 6.7] \cdot 10^{-2}$	$[-6.4, 8.5] \cdot 10^{-2}$	$v^2\, \tilde{c}_{Wb}$	$[-4.2, 4.4] \cdot 10^{-3}$	$[-16, 34] \cdot 10^{-2}$
$v^2\, c_g$	$[-1.7, 1.4] \cdot 10^{-2}$	$[-6.7, 1.1] \cdot 10^{-2}$	$v^2\, \tilde{c}_g$	$[-2.9, 2.9] \cdot 10^{-4}$	$[-2.0, 4.4] \cdot 10^{-2}$
$v^2\, c_Y$	$[-12, 14] \cdot 10^{-2}$	$[-11, 52] \cdot 10^{-2}$	$v^2\, \tilde{c}_Y$	$[-1.3, 1.3] \cdot 10^{-2}$	$[-24, 50] \cdot 10^{-2}$

Table 14: Allowed regions (90% C.L.) for the couplings C_α, at the scale $\Lambda = 1$ TeV, while employing the 'central' strategy outlined in Section 9.2. The second and fifth columns show the constraints when assuming only a single complex coupling is generated at the high scale, while in the third and sixth columns we assume all C_α are present at the scale of new physics and marginalize over the remaining couplings.

both lattice QCD and nuclear many-body theory regarding various matrix elements (see the discussion in Ref. [51]) would be sufficient to make this a realistic scenario.

9.2.1 Global analysis: central values of the hadronic matrix elements

Figs. 5 - 6 show the marginalized constraints as well as those resulting from the single-coupling analysis (at 90% C.L.), using the central procedure in both cases. We immediately notice that the limits on $\tilde{c}_\alpha$ weaken considerably because the imaginary parts of the couplings are strongly correlated. The bounds on $v^2\tilde{c}_\gamma$ and $v^2\tilde{c}_{Wt}$ deteriorate from the few permil level to about 40%. This can be understood from the fact that the electron EDM, which provides the strongest bound in the single operators analysis, is sensitive to the combination $\sim \tilde{c}_\gamma - \tilde{c}_{Wt}$, leaving the orthogonal linear combination unconstrained. This is illustrated in Fig. 7. The required orthogonal constraint comes from δ^-, which only receives contributions from $v^2\tilde{c}_{Wt}$ and is therefore unaffected by marginalizing. The combination of the two then provides the

$\sim 40\%$ bounds on $\tilde{c}_{\gamma,Wt}$. The resulting constraint on $\tilde{c}_\gamma$ is still somewhat stronger than the bound from $b \to s\gamma$. On the other hand, in the marginalized case there are not enough EDM measurements to constrain $\tilde{c}_{Wt}$, and the bound becomes almost identical to that of the direct observable δ^-.

The couplings $\tilde{c}_{Wb}$ and $\tilde{c}_g$ also exhibit strong correlations, because they mainly contribute to the neutron EDM. In the marginalized case, due to the possible cancellations, the bound on $\tilde{c}_{Wb}$ is then mainly determined by A_{CP}, while d_n and $d_{\rm Hg}$ set strong constraints on $\tilde{c}_g$. Similarly, the bound on $\tilde{c}_Y$ is weakened and now allows for a large top pseudoscalar Yukawa coupling, up to 50% of the SM top Yukawa. This further motivates direct searches for CP-odd effects, for instance in the measurements of triple correlations in $t\bar{t}h$ production [43], which can become sensitive to $v^2\tilde{c}_Y \sim \mathcal{O}(0.3)$ at the LHC Run II. The current situation could also be improved by additional EDM experiments. For instance, a proton or deuteron EDM measurement at the level of $d_{p,D} \leq 3.0 \cdot 10^{-26} e$ cm, would significantly shrink the allowed region in the $\tilde{c}_g - \tilde{c}_Y$ plane [51].

The real parts of the coefficients C_α are much less affected by considering multiple operators at the new physics scale Λ. The bounds on c_γ, c_{Wt} and c_{Wb}, which are respectively dominated by $h \to \gamma\gamma$, the W boson helicity fractions and $b \to s\gamma$, are barely changed, and these couplings are nearly uncorrelated. In the single coupling analysis, gluon fusion provides the strongest constraints on both c_g and c_Y. Turning on both couplings therefore allows for cancellations that weaken the bound. The center and right panels of Fig. 6 show that the marginalized bounds on c_g and c_Y from gluon fusion are still better than the individual direct bounds from $t\bar{t}$ and $t\bar{t}h$. The bound on c_g also remains strong in the marginalized case, while cancellations between c_g and c_Y allow for large corrections to the top Yukawa, up to 50%. As is illustrated in Fig. 8, an improved direct measurement of $t\bar{t}h$ at the LHC Run 2, with uncertainties reduced to the 30% - 40% level, would improve the upper bound on c_Y by a factor ~ 2.

The 90% C.L. limits resulting from the marginalized central analysis are summarized, and compared to the individual bounds, in Table 14. Finally, we give some information about the fit. The correlation matrix of the couplings $\{c_\gamma, c_{Wt}, c_{Wb}, c_g, c_Y, \tilde{c}_\gamma, \tilde{c}_{Wt}, \tilde{c}_{Wb}, \tilde{c}_g, \tilde{c}_Y\}$ is given by

$$\left[\begin{array}{rrrrr|rrrrr}
1.00 & 0.17 & 0.32 & -0.35 & 0.27 & 0.00 & 0.00 & 0.00 & 0.00 & 0.00 \\
0.17 & 1.00 & 0.57 & -0.04 & 0.02 & 0.03 & 0.03 & 0.02 & 0.02 & 0.02 \\
0.32 & 0.57 & 1.00 & -0.14 & 0.11 & 0.02 & 0.01 & -0.04 & -0.03 & -0.03 \\
-0.35 & -0.04 & -0.14 & 1.00 & -0.93 & 0.00 & 0.00 & 0.00 & 0.00 & 0.00 \\
0.27 & 0.02 & 0.11 & -0.93 & 1.00 & 0.00 & 0.00 & 0.00 & 0.00 & 0.00 \\
\hline
0.00 & 0.03 & 0.02 & 0.00 & 0.00 & 1.00 & 1.00 & 0.82 & 0.89 & 0.72 \\
0.00 & 0.03 & 0.01 & 0.00 & 0.00 & 1.00 & 1.00 & 0.86 & 0.92 & 0.78 \\
0.00 & 0.02 & -0.04 & 0.00 & 0.00 & 0.82 & 0.86 & 1.00 & 0.98 & 0.88 \\
0.00 & 0.02 & -0.03 & 0.00 & 0.00 & 0.89 & 0.92 & 0.98 & 1.00 & 0.91 \\
0.00 & 0.02 & -0.03 & 0.00 & 0.00 & 0.72 & 0.78 & 0.88 & 0.91 & 1.00
\end{array}\right] . \qquad (66)$$

The off-diagonal entries connecting the real and imaginary couplings are small indicating that there is little correlation between them. This is not surprising as most observables are only

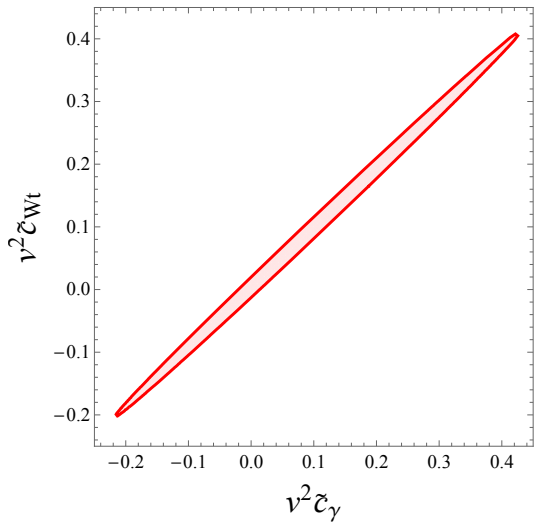

Figure 7: 90% C.L. allowed regions in the $v^2\tilde{c}_\gamma - v^2\tilde{c}_{Wt}$ plane. We marginalized over the remaining couplings and assumed central values for the relevant nuclear and hadronic matrix elements.

sensitive to either the real or the imaginary couplings. The minimum χ^2 of the multidimensional fit is $\chi^2 = 17$, with 45 experimental entries and 10 fit parameters, leading to a χ^2 per degree of freedom, $\chi^2/dof \sim 0.5$.

Table 14 shows that the global fit allows for relative large values of the couplings C_α, especially for the real and imaginary top Yukawa. One might wonder if the EFT approach is still valid in this regime, or if dimension-eight effects, coming for example from double insertions of dimension-six operators, start to become important. By turning on the partial dimension-eight corrections to collider observables and $b \to s\gamma$ given in Sections 4 and 6.1, we checked that the bounds obtained in the global fit with central matrix elements are not significantly affected.

The bounds discussed in this section are obtained under the assumption that only chirality-flipping top-Higgs operators are generated at the new physics scale Λ. Including chirality-conserving top-Higgs operators, such as corrections to the left- and right-handed couplings of the Z boson to the top, or a right-handed coupling of the top to down-type quarks, will not significantly affect the $t\bar{t}$ and $t\bar{t}h$ cross section, or the main Higgs production and decay mechanisms we considered. Thus, we expect the bounds on c_γ, c_g and c_Y not to be significantly altered. On the other hand, single top production, the W polarization in top decay, the S parameter, and $b \to s\gamma$ will receive corrections from chirality-conserving top-Higgs operators of the same importance as the one we included, without additional suppression from small SM couplings. As a result, the bounds on C_{Wt} and C_{Wb} obtained in the global fit might be altered once chirality-conserving operators are added to the high-energy basis. On the other hand, chirality-conserving operators do not induce large contributions to the electron EDM, so that the strong bound on $v^2\tilde{c}_\gamma - v^2\tilde{c}_{Wt}$ shown in Fig. 7 will not be affected.

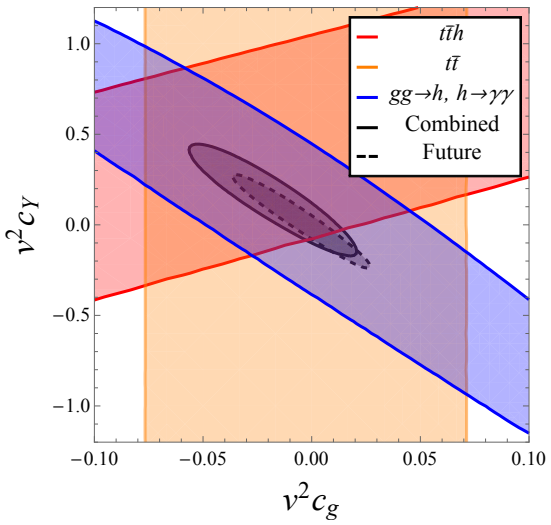

Figure 8: 90% C.L. allowed regions in the $v^2 c_g - v^2 c_Y$ plane, with couplings evaluated at $\Lambda = 1$ TeV. We assume that only C_g and C_Y are generated at the high scale and the theoretical uncertainties are dealt with using the R-fit procedure.

10 Minimal Flavor Violation scenario

In this section we study the top-Higgs couplings in Eq. (2) in the context of Minimal Flavor Violation (MFV) [210]. In the absence of Yukawa couplings of the Higgs to fermions, the SM Lagrangian is invariant under $U(3)^3$ transformations acting on the family indices of the quark fields q_L, u_R, d_R. In the SM, the flavor symmetry $\mathcal{G}_F = SU(3)_{q_L} \times SU(3)_{u_R} \times SU(3)_{d_R}$ is broken by the Yukawa couplings. MFV assumes that this also holds for possible BSM physics and that the only spurions that break $\mathcal{G}_F$ are the Yukawa couplings.

The operators in Eq. (2) all break chiral symmetry. In MFV, their flavor structure is highly constrained and can be obtained by inserting the appropriate combinations of Yukawa matrices Y_u and Y_d that make the operators formally invariant under $\mathcal{G}_F$. For example, to leading order in Yukawa insertions one has $\Gamma^u_{B,W,g}, Y'_u \propto Y_u$ and $\Gamma^d_W \propto Y_d$. More invariants can be constructed by inserting an arbitrary number of products $Y_u Y_u^\dagger$ or $Y_d Y_d^\dagger$, followed by Y_u or Y_d [210]. We restrict ourselves to the case in which only the top Yukawa coupling is treated as $\mathcal{O}(1)$, while the Yukawas of the other quarks are considered small. We then consider operators that contain at most one insertion of light quark Yukawas and an arbitrary number of insertions of y_t. Under this assumption we can disregard insertions of $Y_d Y_d^\dagger$ and it is possible to show that an arbitrary polynomial of $(Y_u Y_u^\dagger)$ induces the same pattern of couplings as a single insertion of $Y_u Y_u^\dagger$.

Within MFV extended by the additional assumptions described above, the chirality-flipping top couplings can only have a limited number of flavor structures. Working in the weak basis in which Y_d is diagonal, $Y_d = \lambda_d$, and $Y_u = V_{\rm CKM}^\dagger \lambda_u$, with $\lambda_d = {\rm diag}(y_d, y_s, y_b)$ and $\lambda_u = {\rm diag}(y_u, y_c, y_t)$, the only possible structures for up-type operators (like C_g, C_γ, C_Y, and C_{Wt}

related to $\Gamma^u_{B,W,g}, Y'_u$) are

$$Y_u = V^\dagger_{\rm CKM}\lambda_u, \qquad P\left(Y_uY_u^\dagger\right)Y_u \sim V^\dagger_{\rm CKM}\begin{pmatrix} 0 & 0 & 0 \\ 0 & 0 & 0 \\ 0 & 0 & y_tP(y_t^2)\end{pmatrix}, \tag{67}$$

where $P(X)$ denotes a polynomial function of X. For down-type operators, like C_{Wb} (related to Γ^b_W) or the b quark dipole moments, we only have

$$Y_d = \lambda_d, \qquad P\left(Y_uY_u^\dagger\right)Y_d \sim P(y_t^2)\cdot\begin{pmatrix} V_{td}V_{td}^*y_d & V_{ts}V_{td}^*y_s & V_{tb}V_{td}^*y_b \\ V_{td}V_{ts}^*y_d & V_{ts}V_{ts}^*y_s & V_{tb}V_{ts}^*y_b \\ V_{td}V_{tb}^*y_d & V_{ts}V_{tb}^*y_s & V_{tb}V_{tb}^*y_b\end{pmatrix}. \tag{68}$$

Rotating the u quark to the mass basis ($u_L \to V^\dagger_{\rm CKM}u_L$), it becomes clear that the operators C_g, C_γ, C_Y, and C_{Wt} correspond to the MFV structure $P\left(Y_uY_u^\dagger\right)Y_u$. The situation is more complicated for the down-type operator C_{Wb}, which does not correspond to any of the structures in Eq. (68), but would be generated by three (or more) insertions of the down Yukawa, $\left(Y_dY_d^\dagger\right)Y_d$, under the assumption that powers of y_d and y_s are small with respect to y_b and can be neglected. We will focus in the rest of this section on up-type operators and neglect C_{Wb}.

Even under the assumption that $y_t \gg y_{u,c}$, we cannot simply set y_u and y_c to zero and reduce the two structures in Eq. (67) to a single one. Instead, we have to consider the scaling of a given observable in powers of the light quark Yukawa couplings. For example, in the case of the nucleon EDM, the first structure in Eq. (67) induces a u quark EDM or CEDM proportional to y_u. As shown in Sec. 3, the second structure also induces u dipoles that are proportional to $y_uy_t^2P(y_t^2)$. Thus the two structures in Eq. (67) contribute to the nucleon EDM at the same order in light quark Yukawas, and are independent.

Thus, in a generic MFV scenario in which arbitrary insertions of y_t are allowed, the operator basis of Eq. (2) needs to be extended

$$\mathcal{L}^{\rm BSM}_{\rm eff} = \sum_{\alpha\in\{Y,g,\gamma,Wt\}} C_\alpha\, O_\alpha + C'_\alpha\, O'_\alpha + \text{h.c.}\,, \tag{69}$$

where

$$O'_Y = -v\,\bar u_L\lambda_u u_R\left(vh + \frac{3}{2}h^2 + \frac{1}{2}\frac{h^3}{v}\right), \tag{70a}$$

$$O'_\gamma = -\frac{eQ_t}{2}v\,\bar u_L\lambda_u\sigma_{\mu\nu}\left(F^{\mu\nu} - t_W Z^{\mu\nu}\right)u_R\left(1+\frac{h}{v}\right), \tag{70b}$$

$$O'_g = -\frac{g_s}{2}v\,\bar u_L\lambda_u\sigma_{\mu\nu}G^{\mu\nu}u_R\left(1+\frac{h}{v}\right), \tag{70c}$$

$$O'_{Wt} = -gv\left[\frac{1}{\sqrt{2}}\bar d_L V^\dagger_{CKM}\lambda_u\sigma^{\mu\nu}u_R W^-_{\mu\nu} + \bar u_L\lambda_u\sigma^{\mu\nu}u_R\left(\frac{1}{2c_W}Z_{\mu\nu} + igW^-_\mu W^+_\nu\right)\right]\left(1+\frac{h}{v}\right) \tag{70d}$$

Coupling	**R-fit**	**Central**
$v^2\tilde{c}'_\gamma$	$[-0.6, 0.6]\cdot 10^{-3}$	$[-4, 4]\cdot 10^{-4}$
$v^2\tilde{c}'_{Wt}$	$[-1.2, 1.2]\cdot 10^{-3}$	$[-3.3, 3.3]\cdot 10^{-4}$
$v^2\tilde{c}'_g$	$[-3.8, 3.8]\cdot 10^{-2}$	$[-0.8, 0.8]\cdot 10^{-5}$
$v^2\tilde{c}'_Y$	$[-1.4, 1.4]\cdot 10^{-2}$	$[-1.3, 1.3]\cdot 10^{-2}$

Table 15: Allowed regions for the couplings $\tilde{c}'_\alpha$ in the linear MFV scenario, under different treatments of the theoretical uncertainties (R-fit versus central).

Differently from the operators $\mathcal{O}_\alpha$, $\mathcal{O}'_\alpha$ induce couplings of the u and c quarks that are proportional to y_u and y_c, respectively. In this context, we wish to address the following questions:

- How do the u and c couplings (implied by linear MFV) affect the constraints on the top-Higgs couplings?
- Do we have enough information to put stringent bounds on the top couplings once we include both flavor structures, C_α and C'_α at the same time?

We focus only on the imaginary parts of the couplings. For the real parts, the best constraints come from top physics, while the u and c couplings are poorly constrained.

To address the first question we assume $C_\alpha = 0$, or equivalently, we work in linear MFV. This assumption is explicitly realized in perturbative models where additional insertions of the Yukawa couplings, such as the structure $(Y_u Y_u^\dagger)Y_u$, are loop suppressed. In Table 15 we list the 90 % C.L. bound on the coefficients $\tilde{c}'_\gamma$, $\tilde{c}'_{Wt}$, $\tilde{c}'_Y$, and $\tilde{c}'_g$, obtained under the assumption of linear MFV, and treating the hadronic uncertainties with the R-fit and central methods. For the R-fit analysis we see that the bound on $\tilde{c}'_\gamma$ is a factor of two stronger than the bound on $\tilde{c}_\gamma$ in Table 13. This can be understood from the tree-level contribution of the u quark EDM to the neutron EDM which does not suffer from hadronic uncertainties because of the good control of the nucleon tensor charges. Furthermore, the charm EDM only provides small contributions to the light quark (C)EDMs and the Weinberg operator, such that there is no room for cancellations.

The bounds on $\tilde{c}'_g$, $\tilde{c}'_{Wt}$, and $\tilde{c}'_Y$ are identical to those on $\tilde{c}_g$, $\tilde{c}_{Wt}$, and $\tilde{c}_Y$ in Table 13, because they are all dominated by the contribution of the top couplings to the electron EDM. The contributions of the u (mainly through the u (C)EDM) and c quark (mainly through the Weinberg operator) to the neutron EDM can cancel with the existing theoretical uncertainties. A comparison with Table 13 reveals that in the central case, the bounds on $\tilde{c}'_\alpha$ are always better than the bounds on c_α, with the exception of the Yukawa coupling. This again illustrates the impact of hadronic uncertainties.

To address the second question, we study the case in which both couplings, C_α and C'_α, are generated by BSM physics. We turn on one class of operators at a time. The top couplings are now proportional to $\tilde{c}_\alpha + \tilde{c}'_\alpha$, while the u and c couplings are proportional to $\tilde{c}'_\alpha$. Strictly speaking there is then no correlation between the top and light flavor couplings. The top anomalous couplings are, because of their contribution to the electron EDM, constrained at the same level as in the non-MFV case. On the other hand, the theoretical uncertainties are large enough that the contributions of the u and c quark to the neutron EDM can cancel, leading to

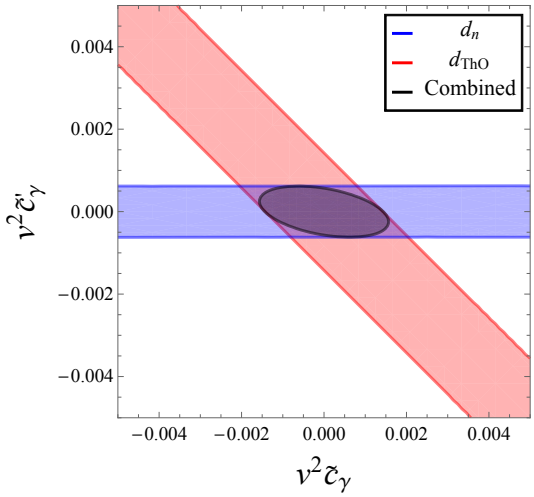

Figure 9: 90% C.L. allowed regions in the $v^2\tilde{c}_\gamma$- $v^2\tilde{c}'_\gamma$ plane, using the R-fit method to treat theoretical uncertainties in the relevant hadronic matrix elements.

no constraint on $\tilde{c}'_\alpha$ with the exception of $\tilde{c}'_\gamma$. For $\tilde{c}_\gamma$ and $\tilde{c}'_\gamma$ we find that both couplings are very well constrained (illustrated in Figure 9)

$$|v^2\tilde{c}_\gamma| < 1.5 \cdot 10^{-3} \qquad |v^2\tilde{c}'_\gamma| < 0.6 \cdot 10^{-3}. \tag{71}$$

For the other couplings, $\tilde{c}_{Wt}$-$\tilde{c}'_{Wt}$, $\tilde{c}_g$-$\tilde{c}'_g$, and $\tilde{c}_Y$-$\tilde{c}'_Y$, there exists a free direction, the direction in which $\tilde{c}_\alpha + \tilde{c}'_\alpha = 0$. Because of the electron EDM limit, the coupling to the top quark remains bound at the same level as in the non-MFV analysis, despite the free direction in the $\tilde{c}_\alpha - \tilde{c}'_\alpha$ plane. Finally, using central values for the matrix elements would lead to bounds on both $\tilde{c}_\alpha$ and $\tilde{c}'_\alpha$ for all couplings.

11 Conclusions

In this work we have discussed probes of chirality-flipping top-Higgs couplings, including both CP-conserving and CP-violating interactions. Working to leading order (dimension-six) in the framework of the SM-EFT, the chirality-flipping interactions involving top and Higgs fields are characterized by five complex couplings. We have studied direct and indirect constraints on these couplings, the latter arising from both high- and low-energy observables (for a synopsis see Tables 6 and 7). We have derived bounds on anomalous couplings under three scenarios: 1) we allow one operator at a time to be generated at the high scale (still allowing for both CP-even and CP-odd couplings). The results of this analysis are summarized in Figs. 3 and 4 and in Table 13. 2) We have performed a global analysis by allowing all chirality-flipping top couplings at the high scale, with results summarized in Figs. 5 and 6 and Table 14. 3) Finally, we have studied the top couplings in the context of Minimal Flavor Violation, which enforces relations among the top and lighter flavor anomalous couplings.

The overarching message emerging from our single-operator analysis is that indirect probes put stronger constraints on the couplings than direct probes. Our major result is that even after properly taking into account the hadronic and nuclear uncertainties, EDMs dominate the

bounds on all the CPV top couplings. In particular, bounds on the top EDM (weak EDM) are improved by three orders of magnitude over the previous literature, leading to $|d_t| < 5 \cdot 10^{-20}$ e cm (90% C.L.). In the Minimal Flavor Violation framework, we find that top CPV couplings are bound at the same level or stronger than in the non-MFV case.

Also for the CP-even couplings we find that indirect probes are very powerful. In the single operator analysis, Higgs production and decay signal strengths, electroweak precision observables, and the $b \to s\gamma$ branching ratio provide better constraints on c_g, c_Y, c_γ, and c_{Wb} than direct observables. The only exception is c_{Wt}, which is mainly constrained by the helicity fractions of W bosons produced in top quark decays.

If BSM physics simultaneously generates several operators at the scale Λ, cancellations are possible. For example, a relatively large top EDM ($\tilde{c}_\gamma$) can be compatible with the absence of a signal in the ThO experiment, if an electron EDM is also generated at the scale Λ, with exactly the right size to cancel the renormalization-group contribution from $\tilde{c}_\gamma$, at the level of a few permil. This implies a very non-trivial conspiracy among the couplings of the underlying model and still sets a powerful constraint on any BSM dynamics.

Another possibility is that new physics generates all the couplings of Eq. (2) at the matching scale Λ. In this case we have quantified the effect of cancellations by performing a global analysis with five complex couplings. For the real part of the couplings we find that most bounds are not significantly affected. The exception are the top chromo-magnetic dipole moment c_g and the correction to the top Yukawa c_Y, whose contributions to Higgs production can conspire to partially cancel. In particular, large corrections to the top Yukawa, up to 50%, are still allowed. Future measurements of the $t\bar{t}$ and $t\bar{t}h$ cross sections at the LHC, especially in regions where the contribution of c_g is enhanced [12], will help to further improve these bounds. For the imaginary part of the couplings, fixing the hadronic and nuclear matrix elements to their central values, we find that the marginalized bounds are one-to-two orders of magnitude weaker than in the single operator analysis. However, as illustrated in Fig. 7, this requires strong correlations among different couplings again pointing to non-trivial effects in the underlying model.

The above conclusions are blurred by a more conservative treatment of theoretical uncertainties, such as the R-fit method. In this case unconstrained directions remain in the ten-dimensional parameter space. In this light, an inclusion of CP-odd collider observables into our analysis would also be very interesting. In any case, the unconstrained directions underscore both the importance of having complementary "orthogonal" probes and the importance of improved calculations of the hadronic and nuclear matrix elements needed to relate EDMs to CP-violating operators.

Acknowledgments – We thank Aneesh Manohar for correspondence on Refs. [55–57], Nicolas Mileo for correspondence on Ref. [43], and we are grateful to Mikołaj Misiak for pointing out Refs. [157, 158] to us. We thank Michael Trott and Alex Pomarol for comments on the manuscript. We also acknowledge stimulating discussions with Sacha Davidson and Joachim Brod. EM thanks Simone Alioli for help in the calculation of the single top cross section. VC and EM acknowledge support by the US DOE Office of Nuclear Physics and by the LDRD program at Los Alamos National Laboratory. WD and JdV acknowledge support by the Dutch Organization for Scientific Research (NWO) through a RUBICON and VENI grant, respectively.

References

[1] CDF, F. Abe *et al.*, Phys. Rev. Lett. **74**, 2626 (1995), hep-ex/9503002.

[2] D0, S. Abachi *et al.*, Phys. Rev. Lett. **74**, 2632 (1995), hep-ex/9503003.

[3] D. B. Kaplan, Nucl. Phys. **B365**, 259 (1991).

[4] K. Agashe, G. Perez, and A. Soni, Phys. Rev. **D75**, 015002 (2007), hep-ph/0606293.

[5] M. Carena, G. Nardini, M. Quiros, and C. E. M. Wagner, Nucl. Phys. **B812**, 243 (2009), 0809.3760.

[6] D. Atwood, A. Aeppli, and A. Soni, Phys. Rev. Lett. **69**, 2754 (1992).

[7] D. Choudhury and P. Saha, JHEP **08**, 144 (2012), 1201.4130.

[8] M. Baumgart and B. Tweedie, JHEP **03**, 117 (2013), 1212.4888.

[9] S. S. Biswal, S. D. Rindani, and P. Sharma, Phys. Rev. **D88**, 074018 (2013), 1211.4075.

[10] W. Bernreuther and Z.-G. Si, Phys. Lett. **B725**, 115 (2013), 1305.2066, [Erratum: Phys. Lett.B744,413(2015)].

[11] Z. Hioki and K. Ohkuma, Phys. Rev. **D88**, 017503 (2013), 1306.5387.

[12] J. A. Aguilar-Saavedra, B. Fuks, and M. L. Mangano, Phys. Rev. **D91**, 094021 (2015), 1412.6654.

[13] J. Bramante, A. Delgado, and A. Martin, Phys. Rev. **D89**, 093006 (2014), 1402.5985.

[14] C. Englert, D. Goncalves, and M. Spannowsky, Phys. Rev. **D89**, 074038 (2014), 1401.1502.

[15] S. D. Rindani, P. Sharma, and A. W. Thomas, JHEP **10**, 180 (2015), 1507.08385.

[16] R. Gaitan, E. A. Garces, J. H. M. de Oca, and R. Martinez, Phys. Rev. **D92**, 094025 (2015), 1505.04168.

[17] W. Bernreuther, D. Heisler, and Z.-G. Si, JHEP **12**, 026 (2015), 1508.05271.

[18] A. Cordero-Cid, J. M. Hernandez, G. Tavares-Velasco, and J. J. Toscano, J. Phys. **G35**, 025004 (2008), 0712.0154.

[19] M. Fael and T. Gehrmann, Phys. Rev. **D88**, 033003 (2013), 1307.1349.

[20] A. O. Bouzas and F. Larios, Phys. Rev. **D87**, 074015 (2013), 1212.6575.

[21] A. O. Bouzas and F. Larios, Phys. Rev. **D88**, 094007 (2013), 1308.5634.

[22] R. Rntsch and M. Schulze, JHEP **08**, 044 (2015), 1501.05939.

[23] B. Grzadkowski and M. Misiak, Phys. Rev. D **78**, 077501 (2008), 0802.1413.

[24] J. Drobnak, S. Fajfer, and J. F. Kamenik, Phys. Rev. **D82**, 114008 (2010), 1010.2402.

[25] G. A. Gonzalez-Sprinberg, R. Martinez, and J. Vidal, JHEP **07**, 094 (2011), 1105.5601, [Erratum: JHEP05,117(2013)].

[26] J. Drobnak, S. Fajfer, and J. F. Kamenik, Nucl. Phys. **B855**, 82 (2012), 1109.2357.

[27] S. D. Rindani and P. Sharma, JHEP **11**, 082 (2011), 1107.2597.

[28] S. D. Rindani and P. Sharma, Phys. Lett. **B712**, 413 (2012), 1108.4165.

[29] Q.-H. Cao, B. Yan, J.-H. Yu, and C. Zhang, (2015), 1504.03785.

[30] Z. Hioki and K. Ohkuma, Phys. Lett. **B752**, 128 (2016), 1511.03437.

[31] R. Romero Aguilar, A. O. Bouzas, and F. Larios, Phys. Rev. **D92**, 114009 (2015), 1509.06431.

[32] M. Schulze and Y. Soreq, (2016), 1603.08911.

[33] J. L. Birman, F. Dliot, M. C. N. Fiolhais, A. Onofre, and C. M. Pease, (2016), 1605.02679.

[34] P. S. Bhupal Dev, A. Djouadi, R. M. Godbole, M. M. Muhlleitner, and S. D. Rindani, Phys. Rev. Lett. **100**, 051801 (2008), 0707.2878.

[35] J. Brod, U. Haisch, and J. Zupan, JHEP **1311**, 180 (2013).

[36] M. J. Dolan, P. Harris, M. Jankowiak, and M. Spannowsky, Phys. Rev. D **90**, 073008 (2014), 1406.3322.

[37] F. Demartin, F. Maltoni, K. Mawatari, B. Page, and M. Zaro, Eur. Phys. J. C **74**, 3065 (2014), 1407.5089.

[38] A. Kobakhidze, L. Wu, and J. Yue, JHEP **10**, 100 (2014), 1406.1961.

[39] S. Khatibi and M. M. Najafabadi, Phys. Rev. D **90**, 074014 (2014), 1409.6553.

[40] F. Demartin, F. Maltoni, K. Mawatari, and M. Zaro, Eur. Phys. J. C **75**, 267 (2015), 1504.00611.

[41] Y. Chen, D. Stolarski, and R. Vega-Morales, Phys. Rev. D **92**, 053003 (2015), 1505.01168.

[42] M. R. Buckley and D. Goncalves, Phys. Rev. Lett. **116**, 091801 (2016), 1507.07926.

[43] N. Mileo, K. Kiers, A. Szynkman, D. Crane, and E. Gegner, (2016), 1603.03632.

[44] J. F. Kamenik, M. Papucci, and A. Weiler, Phys. Rev. D **85**, 071501 (2012), 1107.3143, [Erratum: Phys. Rev.D88,no.3,039903(2013)].

[45] C. Zhang, N. Greiner, and S. Willenbrock, Phys. Rev. **D86**, 014024 (2012), 1201.6670.

[46] J. de Blas, M. Chala, and J. Santiago, JHEP **09**, 189 (2015), 1507.00757.

[47] A. Buckley *et al.*, Phys. Rev. **D92**, 091501 (2015), 1506.08845.

[48] A. Buckley *et al.*, JHEP **04**, 015 (2016), 1512.03360.

[49] O. B. Bylund, F. Maltoni, I. Tsinikos, E. Vryonidou, and C. Zhang, (2016), 1601.08193.

[50] M. Gorbahn and U. Haisch, JHEP **06**, 033 (2014), 1404.4873.

[51] Y. T. Chien, V. Cirigliano, W. Dekens, J. de Vries, and E. Mereghetti, JHEP **02**, 011 (2016), 1510.00725, [JHEP02,011(2016)].

[52] V. Cirigliano, W. Dekens, J. de Vries, and E. Mereghetti, (2016), 1603.03049.

[53] W. Buchmüller and D. Wyler, Nucl. Phys. B **268**, 621 (1986).

[54] B. Grzadkowski, M. Iskrzynski, M. Misiak, and J. Rosiek, JHEP **1010**, 085 (2010), 1008.4884.

[55] E. E. Jenkins, A. V. Manohar, and M. Trott, JHEP **10**, 087 (2013), 1308.2627.

[56] E. E. Jenkins, A. V. Manohar, and M. Trott, JHEP **01**, 035 (2014), 1310.4838.

[57] R. Alonso, E. E. Jenkins, A. V. Manohar, and M. Trott, JHEP **04**, 159 (2014), 1312.2014.

[58] ATLAS, G. Aad *et al.*, JHEP **04**, 023 (2016), 1510.03764.

[59] W. Bernreuther, O. Nachtmann, P. Overmann, and T. Schroder, Nucl. Phys. **B388**, 53 (1992), [Erratum: Nucl. Phys.B406,516(1993)].

[60] A. Brandenburg and J. P. Ma, Phys. Lett. **B298**, 211 (1993).

[61] W. Bernreuther and A. Brandenburg, Phys. Rev. **D49**, 4481 (1994), hep-ph/9312210.

[62] S. Y. Choi, C. S. Kim, and J. Lee, Phys. Lett. **B415**, 67 (1997), hep-ph/9706379.

[63] J. Sjolin, J. Phys. **G29**, 543 (2003).

[64] O. Antipin and G. Valencia, Phys. Rev. **D79**, 013013 (2009), 0807.1295.

[65] S. K. Gupta, A. S. Mete, and G. Valencia, Phys. Rev. **D80**, 034013 (2009), 0905.1074.

[66] S. K. Gupta and G. Valencia, Phys. Rev. **D81**, 034013 (2010), 0912.0707.

[67] A. Hayreter and G. Valencia, Phys. Rev. **D93**, 014020 (2016), 1511.01464.

[68] W. Dekens and J. de Vries, JHEP **1305**, 149 (2013), 1303.3156.

[69] J. Hisano, K. Tsumura, and M. J. Yang, Phys.Lett. **B713**, 473 (2012), 1205.2212.

[70] G. Degrassi, E. Franco, S. Marchetti, and L. Silvestrini, JHEP **0511**, 044 (2005), hep-ph/0510137.

[71] D. B. Kaplan and A. Manohar, Nucl. Phys. B **310**, 527 (1988).

[72] C. Grojean, E. E. Jenkins, A. V. Manohar, and M. Trott, JHEP **1304**, 016 (2013).

[73] T. Bhattacharya, V. Cirigliano, R. Gupta, E. Mereghetti, and B. Yoon, Phys. Rev. **D92**, 114026 (2015), 1502.07325.

[74] J. Elias-Mir, J. R. Espinosa, E. Masso, and A. Pomarol, JHEP **08**, 033 (2013), 1302.5661.

[75] J. Elias-Miro, J. R. Espinosa, E. Masso, and A. Pomarol, JHEP **11**, 066 (2013), 1308.1879.

[76] J. Aebischer, A. Crivellin, M. Fael, and C. Greub, (2015), 1512.02830.

[77] S. Weinberg, Phys. Rev. Lett. **63**, 2333 (1989).

[78] F. Wilczek and A. Zee, Phys. Rev. D **15**, 2660 (1977).

[79] E. Braaten, C.-S. Li, and T.-C. Yuan, Phys. Rev. Lett. **64**, 1709 (1990).

[80] Particle Data Group, K. A. Olive *et al.*, Chin. Phys. **C38**, 090001 (2014).

[81] S. M. Barr and A. Zee, Phys. Rev. Lett. **65**, 21 (1990).

[82] J. Gunion and D. Wyler, Phys.Lett. **B248**, 170 (1990).

[83] T. Abe, J. Hisano, T. Kitahara, and K. Tobioka, JHEP **1401**, 106 (2014), 1311.4704.

[84] M. Jung and A. Pich, JHEP **04**, 076 (2014), 1308.6283.

[85] W. Dekens *et al.*, JHEP **07**, 069 (2014), 1404.6082.

[86] D. A. Dicus, Phys.Rev. **D41**, 999 (1990).

[87] G. Boyd, A. K. Gupta, S. P. Trivedi, and M. B. Wise, Phys.Lett. **B241**, 584 (1990).

[88] M. E. Peskin and T. Takeuchi, Phys. Rev. Lett. **65**, 964 (1990).

[89] M. E. Peskin and T. Takeuchi, Phys. Rev. **D46**, 381 (1992).

[90] R. Barbieri, A. Pomarol, R. Rattazzi, and A. Strumia, Nucl. Phys. **B703**, 127 (2004), hep-ph/0405040.

[91] L. Berthier and M. Trott, JHEP **05**, 024 (2015), 1502.02570.

[92] L. Berthier and M. Trott, JHEP **02**, 069 (2016), 1508.05060.

[93] R. Contino, A. Falkowski, F. Goertz, C. Grojean, and F. Riva, (2016), 1604.06444.

[94] CDF, D0, T. A. Aaltonen *et al.*, Phys. Rev. **D89**, 072001 (2014), 1309.7570.

[95] ATLAS, G. Aad *et al.*, Eur. Phys. J. **C74**, 3109 (2014), 1406.5375.

[96] CMS, S. Chatrchyan *et al.*, JHEP **02**, 024 (2014), 1312.7582, [Erratum: JHEP02,102(2014)].

[97] ATLAS, G. Aad *et al.*, Phys. Rev. **D90**, 112006 (2014), 1406.7844.

[98] CMS, S. Chatrchyan *et al.*, JHEP **12**, 035 (2012), 1209.4533.

[99] CERN Report No. ATLAS-CONF-2014-007, 2014 (unpublished).

[100] CMS, V. Khachatryan *et al.*, JHEP **06**, 090 (2014), 1403.7366.

[101] CERN Report No. ATLAS-CONF-2015-079, 2015 (unpublished).

[102] CERN Report No. CMS-PAS-TOP-16-003, 2016 (unpublished).

[103] D. Atwood, A. Kagan, and T. G. Rizzo, Phys. Rev. **D52**, 6264 (1995), hep-ph/9407408.

[104] P. Haberl, O. Nachtmann, and A. Wilch, Phys. Rev. **D53**, 4875 (1996), hep-ph/9505409.

[105] M. Czakon and A. Mitov, Comput. Phys. Commun. **185**, 2930 (2014), 1112.5675.

[106] M. Czakon, P. Fiedler, and A. Mitov, Phys. Rev. Lett. **110**, 252004 (2013), 1303.6254.

[107] M. Botje *et al.*, (2011), 1101.0538.

[108] H.-L. Lai *et al.*, Phys. Rev. **D82**, 074024 (2010), 1007.2241.

[109] A. D. Martin, W. J. Stirling, R. S. Thorne, and G. Watt, Eur. Phys. J. **C63**, 189 (2009), 0901.0002.

[110] R. D. Ball *et al.*, Nucl. Phys. **B867**, 244 (2013), 1207.1303.

[111] D. Buarque Franzosi and C. Zhang, Phys. Rev. **D91**, 114010 (2015), 1503.08841.

[112] W. Beenakker *et al.*, Phys. Rev. Lett. **87**, 201805 (2001), hep-ph/0107081.

[113] W. Beenakker *et al.*, Nucl. Phys. **B653**, 151 (2003), hep-ph/0211352.

[114] L. Reina and S. Dawson, Phys. Rev. Lett. **87**, 201804 (2001), hep-ph/0107101.

[115] S. Dawson, L. H. Orr, L. Reina, and D. Wackeroth, Phys. Rev. **D67**, 071503 (2003), hep-ph/0211438.

[116] R. Frederix *et al.*, Phys. Lett. **B701**, 427 (2011), 1104.5613.

[117] C. Degrande, J. M. Gerard, C. Grojean, F. Maltoni, and G. Servant, JHEP **07**, 036 (2012), 1205.1065, [Erratum: JHEP03,032(2013)].

[118] A. Hayreter and G. Valencia, Phys. Rev. **D88**, 034033 (2013), 1304.6976.

[119] D0, V. M. Abazov *et al.*, Phys. Rev. Lett. **103**, 092001 (2009), 0903.0850.

[120] CDF, T. Aaltonen *et al.*, Phys. Rev. **D82**, 112005 (2010), 1004.1181.

[121] ATLAS, G. Aad *et al.*, JHEP **01**, 064 (2016), 1510.03752.

[122] CMS, S. Chatrchyan *et al.*, Phys. Rev. Lett. **112**, 231802 (2014), 1401.2942.

[123] CDF, D0, T. A. Aaltonen *et al.*, Phys. Rev. Lett. **112**, 231803 (2014), 1402.5126.

[124] G. Bordes and B. van Eijk, Nucl. Phys. **B435**, 23 (1995).

[125] T. Stelzer, Z. Sullivan, and S. Willenbrock, Phys. Rev. **D56**, 5919 (1997), hep-ph/9705398.

[126] B. W. Harris, E. Laenen, L. Phaf, Z. Sullivan, and S. Weinzierl, Phys. Rev. **D66**, 054024 (2002), hep-ph/0207055.

[127] J. M. Campbell, R. Frederix, F. Maltoni, and F. Tramontano, Phys. Rev. Lett. **102**, 182003 (2009), 0903.0005.

[128] C. Zhang and S. Willenbrock, Phys. Rev. **D83**, 034006 (2011), 1008.3869.

[129] C. Zhang, Phys. Rev. Lett. **116**, 162002 (2016), 1601.06163.

[130] CDF, D0, T. Aaltonen *et al.*, Phys. Rev. **D85**, 071106 (2012), 1202.5272.

[131] ATLAS, G. Aad *et al.*, JHEP **06**, 088 (2012), 1205.2484.

[132] CMS, S. Chatrchyan *et al.*, JHEP **10**, 167 (2013), 1308.3879.

[133] CMS, V. Khachatryan *et al.*, JHEP **01**, 053 (2015), 1410.1154.

[134] J. Boudreau, C. Escobar, J. Mueller, K. Sapp, and J. Su, (2013), 1304.5639.

[135] A. Czarnecki, J. G. Korner, and J. H. Piclum, Phys. Rev. **D81**, 111503 (2010), 1005.2625.

[136] CMS, V. Khachatryan *et al.*, Eur. Phys. J. **C75**, 212 (2015), 1412.8662.

[137] ATLAS, G. Aad *et al.*, Eur. Phys. J. **C76**, 6 (2016), 1507.04548.

[138] LHC Higgs Cross Section Working Group, S. Heinemeyer *et al.*, (2013), 1307.1347.

[139] R. V. Harlander and W. B. Kilgore, Phys. Rev. Lett. **88**, 201801 (2002), hep-ph/0201206.

[140] C. Anastasiou and K. Melnikov, Nucl. Phys. **B646**, 220 (2002), hep-ph/0207004.

[141] V. Ravindran, J. Smith, and W. L. van Neerven, Nucl. Phys. **B665**, 325 (2003), hep-ph/0302135.

[142] C. Anastasiou and K. Melnikov, Phys. Rev. **D67**, 037501 (2003), hep-ph/0208115.

[143] R. V. Harlander and W. B. Kilgore, JHEP **10**, 017 (2002), hep-ph/0208096.

[144] M. Spira, Fortsch. Phys. **46**, 203 (1998), hep-ph/9705337.

[145] B. Grinstein and M. B. Wise, Phys. Lett. **B265**, 326 (1991).

[146] N. Greiner, S. Willenbrock, and C. Zhang, Phys. Lett. **B704**, 218 (2011), 1104.3122.

[147] J. Drobnak, S. Fajfer, and J. F. Kamenik, Phys. Lett. B **701**, 234 (2011), 1102.4347.

[148] P. Mertens and C. Smith, JHEP **08**, 069 (2011), 1103.5992.

[149] S. Bertolini, A. Maiezza, and F. Nesti, Phys. Rev. **D89**, 095028 (2014), 1403.7112.

[150] A. Lenz *et al.*, Phys. Rev. D **83**, 036004 (2011), 1008.1593.

[151] W. Altmannshofer and D. M. Straub, JHEP **08**, 121 (2012), 1206.0273.

[152] W. Altmannshofer, P. Paradisi, and D. M. Straub, JHEP **04**, 008 (2012), 1111.1257.

[153] M. Misiak *et al.*, Phys. Rev. Lett. **98**, 022002 (2007), hep-ph/0609232.

[154] E. Lunghi and J. Matias, JHEP **04**, 058 (2007), hep-ph/0612166.

[155] M. Benzke, S. J. Lee, M. Neubert, and G. Paz, Phys. Rev. Lett. **106**, 141801 (2011), 1012.3167.

[156] A. L. Kagan and M. Neubert, Eur. Phys. J. **C7**, 5 (1999), hep-ph/9805303.

[157] M. Misiak *et al.*, Phys. Rev. Lett. **114**, 221801 (2015), 1503.01789.

[158] M. Czakon *et al.*, JHEP **04**, 168 (2015), 1503.01791.

[159] A. J. Buras, Weak Hamiltonian, CP violation and rare decays, in *Probing the standard model of particle interactions. Proceedings, Summer School in Theoretical Physics, NATO Advanced Study Institute, 68th session, Les Houches, France, July 28-September 5, 1997. Pt. 1, 2*, pp. 281–539, 1998, hep-ph/9806471.

[160] CKMfitter Group, J. Charles *et al.*, Eur. Phys. J. **C41**, 1 (2005), hep-ph/0406184.

[161] Heavy Flavor Averaging Group (HFAG), Y. Amhis *et al.*, (2014), 1412.7515.

[162] ACME Collaboration, J. Baron *et al.*, Science **343**, 269 (2014), 1310.7534.

[163] C. A. Baker *et al.*, Phys. Rev. Lett. **97**, 131801 (2006), hep-ex/0602020.

[164] J. Pendlebury *et al.*, Phys. Rev. **D92**, 092003 (2015), 1509.04411.

[165] W. C. Griffith *et al.*, Phys. Rev. Lett. **102**, 101601 (2009).

[166] B. Graner, Y. Chen, E. G. Lindahl, and B. R. Heckel, (2016), 1601.04339.

[167] K. Kumar, Z.-T. Lu, and M. J. Ramsey-Musolf, Working Group Report: Nucleons, Nuclei, and Atoms, in *Community Summer Study 2013: Snowmass on the Mississippi (CSS2013) Minneapolis, MN, USA, July 29-August 6, 2013*, 2013, 1312.5416.

[168] T. Chupp and M. Ramsey-Musolf, Phys. Rev. **C91**, 035502 (2015), 1407.1064.

[169] M. A. Rosenberry and T. E. Chupp, Phys. Rev. Lett. **86**, 22 (2001).

[170] R. Parker *et al.*, Phys. Rev. Lett. **114**, 233002 (2015), 1504.07477.

[171] V. Baluni, Phys. Rev. D **19**, 2227 (1979).

[172] R. D. Peccei and H. R. Quinn, Phys. Rev. Lett. **38**, 1440 (1977).

[173] M. Pospelov and A. Ritz, Annals Phys. **318**, 119 (2005), hep-ph/0504231.

[174] F. K. Guo *et al.*, Phys. Rev. Lett. **115**, 062001 (2015), 1502.02295.

[175] T. Bhattacharya, V. Cirigliano, R. Gupta, H.-W. Lin, and B. Yoon, Phys. Rev. Lett. **115**, 212002 (2015), 1506.04196.

[176] A. Shindler, T. Luu, and J. de Vries, Phys. Rev. **D92**, 094518 (2015), 1507.02343.

[177] C. Alexandrou *et al.*, Phys. Rev. **D93**, 074503 (2016), 1510.05823.

[178] E. Shintani, T. Blum, T. Izubuchi, and A. Soni, Phys. Rev. **D93**, 094503 (2016), 1512.00566.

[179] J. de Vries, E. Mereghetti, R. G. E. Timmermans, and U. van Kolck, Annals Phys. **338**, 50 (2013), 1212.0990.

[180] J. Bsaisou, U.-G. Meißner, A. Nogga, and A. Wirzba, Annals Phys. **359**, 317 (2015), 1412.5471.

[181] L. V. Skripnikov, A. N. Petrov, and A. V. Titov, The Journal of Chemical Physics **139**, (2013).

[182] T. Fleig and M. K. Nayak, J. Molec. Spectrosc. **300**, 16 (2014), 1401.2284.

[183] PNDME, T. Bhattacharya *et al.*, Phys. Rev. **D92**, 094511 (2015), 1506.06411.

[184] M. Pospelov and A. Ritz, Phys. Rev. D **63**, 073015 (2001), hep-ph/0010037.

[185] O. Lebedev, K. A. Olive, M. Pospelov, and A. Ritz, Phys. Rev. D **70**, 016003 (2004), hep-ph/0402023.

[186] J. Hisano, J. Y. Lee, N. Nagata, and Y. Shimizu, Phys. Rev. D **85**, 114044 (2012), 1204.2653.

[187] D. A. Demir, M. Pospelov, and A. Ritz, Phys. Rev. D **67**, 015007 (2003), hep-ph/0208257.

[188] K. Fuyuto, J. Hisano, and N. Nagata, Phys. Rev. D **87**, 054018 (2013), 1211.5228.

[189] M. Pospelov, Phys. Lett. B **530**, 123 (2002), hep-ph/0109044.

[190] V. F. Dmitriev and R. A. Sen'kov, Phys. Rev. Lett. **91**, 212303 (2003), nucl-th/0306050.

[191] J. H. de Jesus and J. Engel, Phys. Rev. **C72**, 045503 (2005), nucl-th/0507031.

[192] S. Ban, J. Dobaczewski, J. Engel, and A. Shukla, Phys. Rev. **C82**, 015501 (2010), 1003.2598.

[193] V. A. Dzuba, V. V. Flambaum, and S. G. Porsev, Phys. Rev. A **80**, 032120 (2009), 0906.5437.

[194] J. Engel, M. J. Ramsey-Musolf, and U. van Kolck, Prog. Part. Nucl. Phys. **71**, 21 (2013), 1303.2371.

[195] JEDI, D. Eversmann *et al.*, Phys. Rev. Lett. **115**, 094801 (2015), 1504.00635.

[196] J. de Vries *et al.*, Phys. Rev. C **84**, 065501 (2011), 1109.3604.

[197] J. Bsaisou *et al.*, JHEP **03**, 104 (2015), 1411.5804, [Erratum: JHEP05,083(2015)].

[198] I. Stetcu, C.-P. Liu, J. L. Friar, A. C. Hayes, and P. Navratil, Phys.Lett. **B665**, 168 (2008), 0804.3815.

[199] Y.-H. Song, R. Lazauskas, and V. Gudkov, Phys.Rev. **C87**, 015501 (2013), 1211.3762.

[200] N. Yamanaka and E. Hiyama, Phys. Rev. **C91**, 054005 (2015), 1503.04446.

[201] N. Yamanaka, T. Yamada, E. Hiyama, and Y. Funaki, (2016), 1603.03136.

[202] D. Hanneke, S. Fogwell, and G. Gabrielse, Phys. Rev. Lett. **100**, 120801 (2008), 0801.1134.

[203] Muon g-2, G. W. Bennett *et al.*, Phys. Rev. **D73**, 072003 (2006), hep-ex/0602035.

[204] T. Aoyama, M. Hayakawa, T. Kinoshita, and M. Nio, Phys. Rev. Lett. **109**, 111807 (2012), 1205.5368.

[205] R. Bouchendira, P. Clade, S. Guellati-Khelifa, F. Nez, and F. Biraben, Phys. Rev. Lett. **106**, 080801 (2011), 1012.3627.

[206] SuperB, M. Bona *et al.*, (2007), 0709.0451.

[207] S. Nishida, Experimental Prospects for $B \to X_{s/d}\gamma$ and $B- > X_s\ell^+\ell^-$, in *CKM unitarity triangle. Proceedings, 6th International Workshop, CKM 2010, Warwick, UK, September 6-10, 2010*, 2011, 1102.1045.

[208] CMS, Projected Performance of an Upgraded CMS Detector at the LHC and HL-LHC: Contribution to the Snowmass Process, in *Community Summer Study 2013: Snowmass on the Mississippi (CSS2013) Minneapolis, MN, USA, July 29-August 6, 2013*, 2013, 1307.7135.

[209] CERN Report No. ATL-PHYS-PUB-2014-016, 2014 (unpublished).

[210] G. D'Ambrosio, G. Giudice, G. Isidori, and A. Strumia, Nucl.Phys. **B645**, 155 (2002), hep-ph/0207036.